



Local versus global stress constraint strategies in topology optimization: a comparative study

Assis da Silva, Gustavo; Aage, Niels; Beck, André Teófilo; Sigmund, Ole

Published in:
International Journal for Numerical Methods in Engineering

Link to article, DOI:
[10.1002/nme.6781](https://doi.org/10.1002/nme.6781)

Publication date:
2021

Document Version
Peer reviewed version

[Link back to DTU Orbit](#)

Citation (APA):
Assis da Silva, G., Aage, N., Beck, A. T., & Sigmund, O. (2021). Local versus global stress constraint strategies in topology optimization: a comparative study. *International Journal for Numerical Methods in Engineering*, 122(21), 6003-6036. <https://doi.org/10.1002/nme.6781>

General rights

Copyright and moral rights for the publications made accessible in the public portal are retained by the authors and/or other copyright owners and it is a condition of accessing publications that users recognise and abide by the legal requirements associated with these rights.

- Users may download and print one copy of any publication from the public portal for the purpose of private study or research.
- You may not further distribute the material or use it for any profit-making activity or commercial gain
- You may freely distribute the URL identifying the publication in the public portal

If you believe that this document breaches copyright please contact us providing details, and we will remove access to the work immediately and investigate your claim.

RESEARCH ARTICLE

Local versus global stress constraint strategies in topology optimization: a comparative study

Gustavo Assis da Silva*¹ | Niels Aage² | André Teófilo Beck¹ | Ole Sigmund²

¹Department of Structural Engineering, São Carlos School of Engineering, University of São Paulo, 13.566-590, São Carlos, SP, Brazil

²Department of Mechanical Engineering, Solid Mechanics, Technical University of Denmark, Nils Koppels Alle, B. 404, 2800 Kgs. Lyngby, Denmark

Correspondence

*Gustavo Assis da Silva, Department of Structural Engineering, São Carlos School of Engineering, University of São Paulo, 13.566-590, São Carlos, SP, Brazil.

Email: gustavoas@usp.br

Summary

Stress-constrained topology optimization requires techniques for handling thousands to millions of stress constraints. This work presents a comprehensive numerical study comparing local and global stress constraint strategies in topology optimization. Four local and four global solution strategies are presented and investigated. The local strategies are based on either the Augmented Lagrangian or the pure Exterior Penalty method, whereas the global strategies are based on the P -mean aggregation function. Extensive parametric studies are carried out on the L-shaped design problem to identify the most promising parameters for each solution strategy. It is found that: (1) the local strategies are less sensitive to the continuation procedure employed in standard density-based topology optimization, allowing achievement of better quality results using less iterations when compared to the global strategies; (2) the global strategies become competitive when P values larger than 100 are employed, but for this to be possible a very slow continuation procedure should be used; (3) the local strategies based on the Augmented Lagrangian method provide the best compromise between computational cost and performance, being able to achieve optimized topologies at the level of a pure P -continuation global strategy with $P = 300$, but using less iterations.

KEYWORDS:

Topology optimization; Local stress constraints; Global stress constraint; Augmented Lagrangian; Stress aggregation function

1 | INTRODUCTION

Stress-based design is an important field of research in continuum mechanics and topology optimization. Global design criteria such as structural compliance have attractive mathematical properties, allowing efficient topology design using standard sequential convex programming methods as the Method of Moving Asymptotes (MMA) by Svanberg¹; yet, compliance-based formulations do not cover all real engineering applications. In practice, structural design problems are subject to several types of design constraints and among them there are often local stress failure criteria.

In the literature it is acknowledged that, from a physical point of view, stress-constrained problems are essentially different from compliance-based problems. While the latter presents a much simpler formulation, the former presents well-known challenges inherent to the stress constraints and to the fixed grid representation of the design domain: (1) the local nature of the stress

This article has been accepted for publication and undergone full peer review but has not been through the copyediting, typesetting, pagination and proofreading process which may lead to differences between this version and the Version of Record. Please cite this article as doi: 10.1002/nme.6781

Accepted Article

failure criterion; (2) the singularity phenomenon; and (3) the artificial stress concentration at the jagged interfaces between solid and void phases²⁻⁵.

One of the challenges in solving stress-constrained problems using very fine meshes is the local nature of the stress failure criterion, which implies a large number of stress constraints in the discretized model. Usually, there is one stress constraint per element in the mesh, resulting in optimization problems with very large numbers of design variables and constraints. From a computational point of view, topology optimization problems subjected to global failure criteria are much easier to solve, since the sensitivity analysis is performed at the cost of one adjoint problem only, allowing use of the MMA to solve the problem efficiently. The stress-constrained problem, on the other hand, is not trivial and requires use of some strategy to handle the large number of constraints, in order to avoid the gradient computation of each stress constraint individually, which in turn would be impracticable for industrial applications.

Nowadays there are several techniques for handling this difficulty, the most popular ones being global aggregation techniques⁶. The strategy behind aggregation techniques is quite simple: first, the original formulation is rewritten by limiting the maximum stress value instead of the local stresses at all domain points; then, a smooth maximum approximation as the P -norm function is employed to replace the maximum operator, allowing sensitivity analysis at the cost of one adjoint problem only. In order to properly represent the original problem, however, high values of P should be used, which may lead to oscillations and failure of the optimization procedure⁶. Verbart et al.⁷ have demonstrated that one can employ high values as $P = 60$ to address the problem using either the P -mean or the lower bound Kreisselmeier-Steinhauser (KS) function providing nice results, although smaller values as $P = 40$ are suggested by the authors to ensure numerical stability. Alternatively, Le et al.³, París et al.⁸ and Holmberg et al.⁹ have proposed use of regional stress measures, where the constraints are aggregated into smaller groups instead of into a single global constraint, allowing use of lower values of P to address the problem, with the drawback of requiring solution of additional adjoint problems to perform the sensitivity analysis.

Another approach, that has become more popular recently, is to address the original problem with all local stress constraints by means of the Augmented Lagrangian (AL) method, i.e., without employing aggregation techniques. Use of the AL method to handle the stress-constrained problem was proposed by Fancello and Pereira¹⁰ and Pereira et al.¹¹; the authors have demonstrated that one can exploit the AL formulation to address the original problem, with all local stress constraints, in order to solve the problem efficiently at the cost of one adjoint problem only to perform the sensitivity analysis. Since then, the AL method has been used to address several kinds of stress-constrained problems in the literature, using the density-based¹²⁻¹⁹ and level-set²⁰⁻²³ methods. Also, the AL method was recently employed to solve truly large-scale topology optimization problems with hundreds of millions of local stress constraints providing excellent results in reasonable computational time, proving AL to be a very promising method and motivating its application at industrial level²⁴.

In this paper, a numerical comparison between global solution strategies based on the P -mean function and local solution strategies based on the AL method is presented. The P -mean function is chosen instead of the P -norm as it leads to a smooth maximum approximation whose error of estimation is less dependent on the number of input arguments. Following Fernández et al.²⁵, for the same data distribution, the amount of data does not affect the P -mean function, but it affects the P -norm, justifying the mesh independent behavior of the P -mean approach for topology optimization problems with maximum length scale constraint addressed in their paper. All global and local approaches addressed in the manuscript are promising in the sense that optimization can be carried out efficiently, at the cost of a single adjoint analysis per iteration. Four variants of global aggregation strategies and four variants of local solution strategies are considered, and extensive numerical studies are carried out to identify the most promising approaches among them.

A comprehensive literature review revealed few papers presenting comparisons between local and global strategies for stress-constrained topology design. A comparison is presented by París et al.²⁶, who found that the local strategy is more robust and provides better results, with the drawback of higher computational cost due to the necessity of computing the gradient of each constraint individually; in their paper, however, they do not address the AL method to handle the local stress constraints. More recently, de Assis Pereira and Cardoso²⁷ have presented a numerical comparison between the local strategy using the AL method and the global strategy using the P -norm function for stress-constrained compliant mechanism design. In reference²⁷, however, global stress-constrained optimization problems are solved using the AL method, whereas the MMA is more frequently employed. Moreover, the Optimality Criteria method²⁸ is employed in reference²⁷ to solve the AL optimization subproblems, instead of more general mathematical programming algorithms. This prevents its extension to alternative optimization problems such as the volume minimization problem with stress constraint addressed in the current manuscript.

In this paper, we present a comprehensive comparison between local and global stress constraint strategies with three main differences compared to references^{26,27}:

1. The local strategies are based on either the AL method or the pure Exterior Penalty (EP) method. We thus investigate the influence/necessity of using Lagrange multipliers in the local approaches.
2. Two optimization methods are employed to solve the optimization subproblems of the AL and EP methods: MMA and Steepest Descent method with Move limits (SDM)^{24,29}. Both are general mathematical programming tools, allowing extension of the stress constraints handling strategy to different optimization problems.
3. The optimization problems with global stress constraint are solved with the MMA, which is the standard tool in the field of topology optimization, as seen in the literature. Using this method allows more competitive comparisons, since P values as high as 300 could be employed when using the P -mean function to smooth the maximum operator.

The paper is organized as follows. Section 2 presents the local and global stress-constrained formulations. Section 3 presents the four local and four global solution strategies addressed in this paper. Section 4 presents a parametric study performed on the eight solution strategies. Section 5 discusses practical stopping criteria and how to ensure stress constraint feasibility. Section 6 presents numerical results and important insights. Section 7 summarizes the main conclusions of this study. Appendix A presents additional details regarding the solution procedure. Appendix B presents the sensitivity analyses. Appendix C presents complementary numerical results. Finally, Appendix D presents the iteration histories related to the parametric studies.

2 | STRESS-CONSTRAINED TOPOLOGY OPTIMIZATION

In this paper, stress-constrained volume minimization problems are addressed^{3,30}. The goal is to find the topology of minimum structural volume that satisfies the stress failure criterion at all points of the design domain. In this section, two optimization formulations that seek this goal are presented: (1) the local stress-constrained formulation, which is defined by applying one constraint on each stress computation point, subsection 2.1; and (2) the global stress-constrained formulation, which is defined by applying a single constraint on the point with maximum stress value, subsection 2.2.

The density approach to topology optimization is employed to formulate both problems³¹: the design domain is discretized with a fixed mesh of finite elements (Eulerian approach), and each element is associated with a continuous relative density, $\bar{\rho}_e$, which may take values from 0 (void phase) to 1 (solid phase). The topology design is then performed by an iterative process which uses some gradient-based numerical optimization method to update the relative densities, as described in section 3. The density filter with threshold projection is applied to compute the relative densities in both formulations, as defined in subsection 2.1.

The local and global stress-constrained problems are formulated by employing the same base interpolation functions and governing parameters (e.g., stiffness and stress interpolation functions) as defined in subsection 2.1. The von Mises stress failure criterion is used, and hypothesis of linear elasticity under static loads is considered. The standard displacement-based finite element method is employed for structural analysis³². The systems of linear equations resulting from the state and adjoint problems are solved with the multigrid preconditioned CG³³. A V-cycle framework with four multigrid levels is employed, with a single damped Jacobi smoothing step per level (damping factor of 0.8) and a relative convergence tolerance of 10^{-5} . A direct solve is performed on the coarse-level problem.

2.1 | Local stress-constrained formulation

The volume minimization problem with local stress constraints in discrete form is written as

$$\begin{aligned}
 \text{Min.}_{\bar{\rho}} \quad & V_f(\bar{\rho}) = \frac{\sum_{e=1}^{N_e} V_e \bar{\rho}_e}{\sum_{e=1}^{N_e} V_e} \\
 \text{s. t.} \quad & \frac{\sigma_{eq}^{(k)}(\bar{\rho})}{f_\alpha(\sigma_y)} - 1 \leq 0 \quad k = 1, 2, \dots, N_k, \\
 & \mathbf{K}(\bar{\rho}) \mathbf{U}(\bar{\rho}) = \mathbf{F} \\
 & 0 \leq \rho_e \leq 1 \quad e = 1, 2, \dots, N_e
 \end{aligned} \tag{1}$$

where $V_f(\bar{\rho})$ is the volume fraction of the structure with respect to the design domain, $\bar{\rho} \in \mathbb{R}^{N_e}$ are the relative densities, V_e is the volume of element e , $\bar{\rho}_e$ is the relative density of element e , N_e is the number of elements in the mesh, $\sigma_{eq}^{(k)}(\bar{\rho})$ is the von Mises equivalent stress at point k , $f_\alpha(\sigma_y)$ is the yield stress function, N_k is the number of von Mises stress computation points,

$\mathbf{K}(\bar{\rho})$ is the global stiffness matrix, $\mathbf{U}(\bar{\rho})$ is the global displacement vector, \mathbf{F} is the global load vector and ρ_e is the design variable associated with element e . The local stiffness matrix of element e is computed with the Solid Isotropic Material with Penalization (SIMP) scheme²⁸, as $\mathbf{k}_e(\bar{\rho}_e) = (\rho_{min} + (1 - \rho_{min}) \bar{\rho}_e^p) \mathbf{k}_e^0$, where \mathbf{k}_e^0 is the local stiffness matrix of base material of element e , $\rho_{min} = 10^{-9}$ is adopted to avoid singularity issues when solving for equilibrium, and $p = 3$ is used as penalization factor.

The yield stress function is given by $f_\alpha(\sigma_y) = \alpha\sigma_y$, where σ_y is the yield stress and $\alpha \leq 1$ is the yield stress reduction factor. The reduction factor is employed in this manuscript to handle small tolerance values that may arise from the numerical optimization process, helping to ensure stress constraint feasibility at the final steps of the iterative procedure, i.e., $\sigma_{eq}^{(k)}(\bar{\rho}) \leq \sigma_y$ for $k = 1, 2, \dots, N_k$. The value of α is defined based on numerical experiments and is given in section 5 for different solution strategies, being within range $\alpha \in [0.97, 1.00]$ for the problems addressed in this manuscript.

The von Mises equivalent stress is computed based on Duysinx and Bendsøe², and is written as

$$\begin{aligned} \sigma_{eq}^{(k)}(\bar{\rho}) &= f_\sigma(\bar{\rho}_k) \hat{\sigma}_{eq}^{(k)}(\bar{\rho}) \\ &= f_\sigma(\bar{\rho}_k) \sqrt{\hat{\sigma}_k^T(\bar{\rho}) \mathbf{M} \hat{\sigma}_k(\bar{\rho}) + \sigma_{min}^2}, \end{aligned} \quad (2)$$

where $f_\sigma(\bar{\rho}_k)$ is the stress interpolation function, $\hat{\sigma}_{eq}^{(k)}(\bar{\rho})$ is the solid von Mises stress at point k , $\hat{\sigma}_k(\bar{\rho})$ is the solid stress vector at point k in Voigt notation, $\sigma_{min} = 10^{-4}\sigma_y$ is a small value included in our implementations to ensure a positive von Mises equivalent stress when $\hat{\sigma}_k^T(\bar{\rho}) \mathbf{M} \hat{\sigma}_k(\bar{\rho}) \rightarrow 0$, thus avoiding numerical instabilities during the sensitivity analysis, and \mathbf{M} is the standard operator matrix for calculating the von Mises stresses.

The solid stress vector is given by

$$\hat{\sigma}_k(\bar{\rho}) = \mathbf{C}^0 \mathbf{B}_k \mathbf{u}_k(\bar{\rho}), \quad (3)$$

where \mathbf{C}^0 is the constitutive matrix of the base material, \mathbf{B}_k is the strain-displacement transformation matrix evaluated at point k and $\mathbf{u}_k(\bar{\rho})$ is the local displacement vector of the element which contains point k .

The stress interpolation function, $f_\sigma(\bar{\rho}_k)$, is chosen to avoid the singularity phenomenon³ and to ensure stress accuracy at the interfaces between solid and void phases⁵. In this paper, the ϵ -relaxed approach is employed^{6,34}, with $f_\sigma(\bar{\rho}_k) = \frac{\bar{\rho}_k}{\epsilon(1-\bar{\rho}_k)+\bar{\rho}_k}$. Da Silva et al.⁵ demonstrated, through numerical investigation, that parameter ϵ , when associated with a smooth transition boundary of proper thickness between solid and void phases, can be chosen to ensure stress accuracy at topology boundaries when these are not aligned with the fixed background mesh. Following da Silva et al.⁵, we choose $\epsilon = 0.2$. Body-fitted verification of several stress-constrained results using $\epsilon = 0.2$ is performed by da Silva et al.^{5,14,16,24}, and results in less than 10% error between fixed grid and body-fitted maximum von Mises stresses.

Relative densities are obtained through a density filter with threshold projection. The threshold projection relates relative densities to filtered densities and is given by³⁵

$$\bar{\rho}_e = \frac{\tanh(\beta\eta) + \tanh(\beta(\tilde{\rho}_e - \eta))}{\tanh(\beta\eta) + \tanh(\beta(1 - \eta))}, \quad (4)$$

where $\tilde{\rho}_e$ is the filtered density of element e , $\eta \in (0, 1)$ controls the inflection point of the threshold projection, chosen as $\eta = 0.5$ in this paper, and $\beta > 0$ controls the sharpness of the projection: the larger the value of β , the smaller the amount of intermediate material in the topology.

Filtered densities, $\tilde{\rho}$, are obtained implicitly by solving a Partial Differential Equation (PDE) with homogeneous Neumann boundary conditions³⁶, given by

$$-\left(\frac{R}{2\sqrt{3}}\right)^2 \nabla^2 \tilde{\rho} + \tilde{\rho} = \rho, \quad \frac{\partial \tilde{\rho}}{\partial \mathbf{n}} = 0, \quad (5)$$

where $R \geq 0$ is the filter radius.

As discussed in da Silva et al.⁵, the value of β plays an important role in accuracy of stress computation when using standard fixed grid approaches in topology design. It was found that a thin layer of smooth transition boundary between solid and void regions, when associated with proper stiffness and stress interpolation functions, is beneficial for improving the stress accuracy at topology boundaries. It was demonstrated that a transition thickness with size equal to or larger than twice the side length l_e of an element of a grid-like mesh improves the stress accuracy when associated with $p = 3$ (SIMP) and $\epsilon = 0.2$ (ϵ -relaxation). This transition thickness can be achieved by considering $\beta \cong \beta_{lim}^{PDE}/2$ in Equation (4), where $\beta_{lim}^{PDE} = \frac{2R}{l_e\sqrt{3}}$ for the PDE-based filter²⁴. This value of β , however, is not applied directly to the problem, but gradually approached through a continuation approach instead, as presented in section 3.

2.2 | Global stress-constrained formulation

An equivalent alternative to the formulation with local constraints, Equation (1), consists of replacing all the stress constraints with their maximum value, resulting in a formulation with a single global stress constraint, written as

$$\begin{aligned} \text{Min. } & V_f(\bar{\rho}) \\ \text{s. t. } & \frac{\max\{\sigma_{eq}(\bar{\rho})\}}{f_e(\sigma_e)} - 1 \leq 0, \\ & \mathbf{K}(\bar{\rho}) \mathbf{U}(\bar{\rho}) = \mathbf{F} \\ & 0 \leq \rho_e \leq 1 \quad e = 1, 2, \dots, N_e \end{aligned} \quad (6)$$

where $\max\{\sigma_{eq}(\bar{\rho})\} = \max\{\sigma_{eq}^{(1)}(\bar{\rho}), \sigma_{eq}^{(2)}(\bar{\rho}), \dots, \sigma_{eq}^{(N_k)}(\bar{\rho})\}$.

Replacing the local stress constraints with a single global constraint may be attractive from a computational point of view, since the gradient computation of a single constraint can be performed efficiently through adjoint analysis, instead of computing the gradient of each local constraint individually. Using the maximum operator, however, prevents use of standard gradient-based optimization methods, since it is non-differentiable. A simple and effective way to solve this issue is to replace the maximum operator with a smooth approximation; using this strategy in stress-constrained continuum topology optimization was proposed by Duysinx and Sigmund⁶, which presented the P -norm and P -mean aggregation functions as valid alternatives. The authors have discussed the compromise relation between accuracy and numerical stability: the value of P should be large enough to properly capture the maximum von Mises stress value; yet, the value of P should be small enough to ensure numerical stability and avoid divergence of the optimization procedure due to excessive nonlinearity.

Since the seminal work by Duysinx and Sigmund⁶, global stress-constrained formulations with smoothing by aggregation functions have become one of the most popular approaches to handle stress constraints in continuum topology optimization (see, e.g., references^{37–46}). Nowadays, there are plenty of alternative aggregation functions and solution strategies that can be employed to address the problem, the most popular ones being the P -norm/ P -mean and upper/lower bound KS functions.

In this work, the P -mean function is employed to smooth the maximum operator of Equation (6); the global stress-constrained problem with the P -mean aggregation function is written as

$$\begin{aligned} \text{Min. } & V_f(\bar{\rho}) \\ \text{s. t. } & \left[\frac{1}{N_k} \sum_{k=1}^{N_k} \left(\frac{\sigma_{eq}^{(k)}(\bar{\rho})}{f_e(\sigma_e)} \right)^P \right]^{\frac{1}{P}} - 1 \leq 0, \\ & \mathbf{K}(\bar{\rho}) \mathbf{U}(\bar{\rho}) = \mathbf{F} \\ & 0 \leq \rho_e \leq 1 \quad e = 1, 2, \dots, N_e \end{aligned} \quad (7)$$

where P is a penalty factor that controls the accuracy of the approximation; for $P \rightarrow \infty$ the maximum value is recovered. What differentiates the P -mean function from the P -norm is the normalization factor $1/N_k$, which is not present in the latter. It is well known that the P -mean underestimates and the P -norm overestimates the maximum value for moderate P , both tending to the maximum as P increases⁶.

Verbart et al.⁷ present a comprehensive discussion between lower and upper bound aggregation functions for stress-constrained topology design; the authors compare the P -mean and lower bound KS functions (both lower bound functions) to the P -norm and upper bound KS functions (both upper bound functions). The authors⁷ found that use of the lower bound aggregation functions to approximate the maximum operator in stress-constrained topology design exempt use of stress constraint relaxation techniques to overcome the singularity phenomenon, in the sense that the lower bound functions naturally provide the combined effect of aggregation and relaxation of the design domain. In this paper, however, we preferred to employ the same stress interpolation function used in the local stress-constrained problem, f_σ in Equation (2), also in this case, in order to maintain the same interpolation functions for local and global cases thus providing a fairer comparison. Investigation of the relaxation effect of using the P -mean function is thus not addressed in this paper.

3 | SOLUTION STRATEGIES

3.1 | Local stress constraints

The four solution strategies developed to handle the local stress-constrained problem are based on either the Augmented Lagrangian (AL) formulation by Birgin and Martínez⁴⁷ or the pure Exterior Penalty (EP) method, which consists of a particularization of the former for null multipliers. In this subsection, the AL formulation is briefly presented and later particularized for the case of pure external penalty.

The AL method works by replacing the original (constrained) optimization problem with a sequence of unconstrained optimization subproblems. The objective function of the optimization subproblems is the AL function, which is a combination of the original objective function and the design constraints in the form of a penalty term. After defining the optimization subproblems, the optimization procedure is performed by solving each subproblem sequentially, using the solution of the previous subproblem as starting point; the procedure is thus performed until the stopping criteria are reached.

In this paper, the AL function is defined using all the stress constraints of the problem, such as

$$L(\boldsymbol{\rho}, \boldsymbol{\mu}, r) = V_f(\bar{\boldsymbol{\rho}}) + \frac{r}{2} \sum_{k=1}^{N_k} \left\langle \frac{\mu_k}{r} + \frac{\sigma_{eq}^{(k)}(\bar{\boldsymbol{\rho}})}{f_\alpha(\sigma_y)} - 1 \right\rangle^2, \quad (8)$$

where $\langle \cdot \rangle = \max\{0, \cdot\}$, r is the penalization parameter, $\boldsymbol{\mu} \in \mathbb{R}^{N_k}$ are the Lagrange multipliers, and μ_k is the Lagrange multiplier associated with k -th stress constraint. The particularization of this formulation to the pure exterior penalty approach is simply performed by considering $\mu_k = 0$, in Equation (8), during the whole optimization procedure.

The optimization subproblems are given by

$$\begin{aligned} \text{Min.}_{\boldsymbol{\rho}} \quad & L(\boldsymbol{\rho}, \boldsymbol{\mu}, r) \\ \text{s. t.} \quad & \mathbf{K}(\bar{\boldsymbol{\rho}}) \mathbf{U}(\bar{\boldsymbol{\rho}}) = \mathbf{F} \\ & 0 \leq \rho_e \leq 1 \quad e = 1, 2, \dots, N_e \end{aligned}, \quad (9)$$

for either AL or pure EP approaches. These are solved with either the SDM or MMA update strategies (see Appendix A). The associated sensitivity analysis is given in Appendix B.1.

3.1.1 | Proposed solution strategies for local stress constraints

The iterative procedure is performed over the optimization subproblems, Equation (9), for AL and EP strategies, using either SDM or MMA update schemes. In the AL method, after solving a given optimization subproblem, the Lagrange multipliers and penalization parameter are updated, i.e., these are updated between the optimization iterations and kept constant within each subproblem. In practice, there is no need to reach the stationary point of each subproblem; good solutions are obtained using a fixed number of iterations per subproblem, as demonstrated in references^{17,20–24}. In this paper, parameters μ_k (k -th Lagrange multiplier), r (penalization parameter), and β (threshold projection) are updated every 20 iterations, using the following relations

$$\mu_k = \left\langle r \left(\frac{\sigma_{eq}^{(k)}(\bar{\boldsymbol{\rho}})}{f_\alpha(\sigma_y)} - 1 \right) + \mu_k \right\rangle, \quad (10)$$

$$r = \min \left\{ \gamma_r r, \frac{r_{max}}{N_k} \right\}, \quad (11)$$

$$\beta = \min \left\{ \gamma_\beta \beta, \beta_{max} \right\}, \quad (12)$$

where γ_r and γ_β are update parameters, and r_{max} and β_{max} are the maximum values employed for penalization and threshold projection, respectively. The maximum penalization parameter is normalized by the number of stress constraints to alleviate mesh dependence effects^{14,24}. Parameters γ_r and γ_β are automatically chosen to achieve $r = \frac{r_{max}}{N_k}$ and $\beta = \beta_{max}$ in $nit_{min} - 20$ iterations, with nit_{min} being the number of iterations employed to perform the continuation procedure. The iterative procedure is started with $\mu_k = 0$, $r = r_0$ and $\beta = \beta_0$. Initial and maximum values for r and β are given in the results section. The choice of updating the numerical parameters every 20 iterations is based on experience. Other update strategies may also be employed to improve results quality, but such investigations are out of the scope of the current work.

The pure EP strategy employs the same update equations for r and β . The difference between AL and EP is that the update equation for μ_k is not used in the latter, hence $\mu_k = 0$ during the whole optimization procedure.

To ease comparisons, we do not define a stopping criterion for the solution algorithm; instead, a maximum number of iterations, nit_{max} , is used. Thus, we seek to compare all approaches for the same minimum and maximum number of iterations.

Based on the above, the following four solution strategies are defined to address the local stress-constrained problem, Equation (1); two based on the AL and two on the pure EP method.

Local 1: AL + SDM. The problem is addressed with the AL method through iterative procedure over the optimization subproblems, Equation (9). The SDM is employed to perform the optimization iterations, with updates to μ_k , r and β every 20 iterations.

Local 2: AL + MMA. Same as Local 1, with MMA instead of SDM to perform the iterations.

Local 3: EP + SDM. Same as Local 1, with EP instead of AL to address the problem. The SDM is employed to perform the optimization iterations, with updates to r and β only, every 20 iterations. $\mu_k = 0$ during the whole optimization procedure.

Local 4: EP + MMA. Same as Local 3, with MMA instead of SDM to perform the iterations.

3.2 | Global stress constraint

The four solution strategies developed to handle the global stress-constrained problem use the MMA to update the design variables. In this case, the closed form update scheme cannot be employed (see Appendix A), since there is a global stress constraint to be handled in addition to the bound constraints. The dual of the MMA subproblem is then solved with an interior point method⁴⁸. The computation strategy employed to set move limits and asymptotes presented in Appendix A is also employed herein to address the global stress-constrained formulation, since it turned out to be necessary to achieve P values as high as 300 in problem with large number of elements ($N_e \cong 400,000$). The associated sensitivity analysis is given in Appendix B.2.

3.2.1 | Proposed solution strategies for global stress constraint

In order to reproduce the original problem with global stress constraint based on the maximum operator, Equation (6), one has to employ P values as large as possible in its smoothed version, Equation (7), thus reducing the gap between the maximum stress value and the P -mean function. Use of too small values of P leads to differences between the original and smoothed versions of the problem, and hence the optimized topology obtained using the smoothed formulation may not be optimized for the original problem based on the maximum operator. On the other hand, using too large values of P may lead to numerical oscillations and divergence of the optimization procedure⁶. Aiming to reduce the gap between maximum and P -mean response values, two approaches are investigated in this paper, as follows.

1. *Adaptive normalization scheme*^{3,49}. A common strategy is to use the adaptive constraint normalization scheme associated with moderate values of P , aiming to reduce the gap between the smoothed aggregation function and the maximum operator while keeping a numerically stable optimization procedure. The normalization scheme consists of rewriting the global stress constraint of Equation (7) as³

$$\tilde{\sigma}_{PM} - 1 \leq 0, \quad (13)$$

where $\tilde{\sigma}_{PM} = c_{PM} \sigma_{PM}$ and $\sigma_{PM} = \left[\frac{1}{N_k} \sum_{k=1}^{N_k} \left(\frac{\sigma_{eq}^{(k)}(\bar{\rho})}{f_\alpha(\sigma_y)} \right)^P \right]^{\frac{1}{P}}$, and then correcting the stress constraint every iteration b using the following equation

$$c_{PM}^{(b)} = q \frac{\max \left\{ \sigma_{eq} \left(\bar{\rho}^{(b-1)} \right) \right\}}{f_\alpha(\sigma_y) \sigma_{PM}^{(b-1)}} + (1 - q) c_{PM}^{(b-1)} \quad (14)$$

where $q \in (0, 1]$ is the control factor, chosen as $q = 0.5$ in this paper, following Yang et al.⁴⁹, and $c_{PM}^{(0)} = 1$. As discussed by Le et al.³, the normalized stress constraint, Equation (13), is non-differentiable, since c_{PM} changes in a discontinuous manner during the optimization process, hence resulting in slightly different optimization problems every iteration. The authors argue, however, that c_{PM} converges as the iterative procedure converges, hence alleviating possible numerical oscillations that may be caused by the non-differentiability of the stress constraint.

2. *P-continuation scheme*⁵⁰. An alternative strategy is to reduce the gap between P -mean and maximum operator by simply using very large values of P during the optimization procedure. In order to make it possible, however, the value of P should

be increased gradually during the optimization procedure, until it reaches its maximum value. In this paper, the following equation is applied every 20 iterations to update the value of P , whenever the P -continuation approach is employed:

$$P = \min \{ \gamma_P P, P_{max} \}, \quad (15)$$

where γ_P is an update parameter and P_{max} is the maximum value employed in the P -mean aggregation function during the optimization procedure. Parameter γ_P is automatically chosen to achieve $P = P_{max}$ in $nit_{min} - 20$ iterations. Initial, P_0 , and maximum values for P are given in the results section.

Based on the two strategies presented above, the following four solution strategies are defined to address the P -mean global stress-constrained problem. All approaches use the MMA to perform the optimization iterations, differing only in the constraint handling strategy and continuation procedure.

Global 1: P -continuation. The problem is solved without employing the adaptive stress normalization scheme. Parameters β and P are updated every 20 iterations with Equations (12) and (15), respectively.

Global 2: P -continuation + c_{PM} normalization (1 it). The problem is solved using the adaptive stress normalization scheme every iteration through application of Equation (14). Parameters β and P are updated every 20 iterations.

Global 3: P -continuation + c_{PM} normalization (20 it). The problem is solved using the adaptive stress normalization scheme every 20 iterations only, together with updates to β and P .

Global 4: Fixed P + c_{PM} normalization (1 it). The P -continuation procedure is not employed. Instead, parameter P is kept constant during the whole optimization procedure, as usually performed in the literature. The problem is solved using the adaptive stress normalization scheme every iteration. Parameter β is updated every 20 iterations.

4 | PARAMETRIC STUDY

A parametric study is performed on the L-shaped design problem to identify the most promising r_{max} and P_{max} values for the four local and four global solution strategies, respectively. The hypothesis of plane stress is considered and four-node square elements are employed. Figure 1 illustrates geometry and boundary conditions. An internal padding region of width equal to R , represented by dashed lines, is employed to alleviate possible boundary effects that may occur due to filtering; this region is filled with design variables equal to zero, and the gradient components at these points are set to zero, following²⁴.

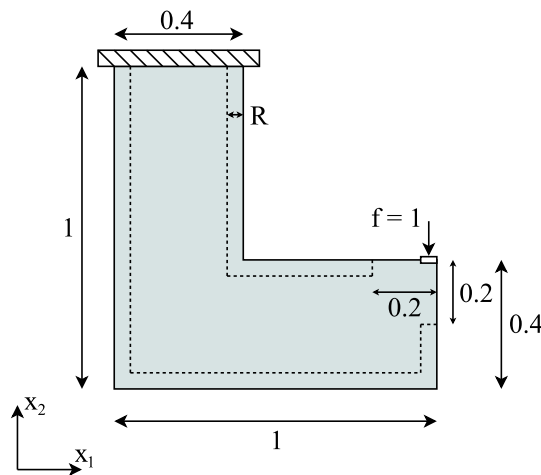


FIGURE 1 L-shaped design domain. The padding region is represented by dashed lines.

Input data are: applied load 1 (distributed over a boundary length of 0.05 to avoid stress singularity), Young's modulus 1, Poisson's ratio 0.3, thickness 1, yield stress $\sigma_y = 70$, filter radius $R = 0.03$, and initial design variables $\rho = 1$ (except at the

internal padding regions). Von Mises equivalent stresses are computed at the centroid of each element, following da Silva et al.⁵, and also in agreement with other papers in the literature^{3,4,7,9,41}. The iterative procedure is carried out according to the eight solution strategies defined in this section; parameters r (local), P (global), and β (local and global) are gradually increased every 20 iterations from $r_0 = \frac{0.01}{N_k}$, $P_0 = 2$, and $\beta_0 = 0.1$, to $\frac{r_{max}}{N_k}$, P_{max} and β_{max} , respectively, with the exception of Global 4 approach, in which parameter P is fixed during the whole optimization procedure, i.e., $P_0 = P_{max} > 2$. Parameters r_0 , P_0 and β_0 are chosen based on numerical experience with the formulations; in general, small values are preferred in the beginning of the optimization process to avoid numerical instabilities during the iterative procedure. Parameter r_0 requires the normalization by N_k to alleviate mesh dependence effects. The maximum value of β is defined based on the finest mesh as $\beta_{max} \cong \frac{R}{l_e \sqrt{3}} \cong 13.856$. In this study, the yield stress function is computed using $\alpha = 1$, i.e., $f_\alpha(\sigma_y) = \sigma_y$, in all cases.

Four r_{max} values are considered for each of the four local solution strategies, whereas four P_{max} values are considered for the global ones. These are employed to solve the problem using two mesh sizes: 200×200 ($N_e = 25,600$) and 800×800 ($N_e = 409,600$); resulting in 64 optimization problems. The optimization process follows the standard β -continuation approach often employed in density-based topology optimization⁵¹, using Equation (12) every 20 iterations, to slowly increase β through the iterative process. In addition to β , parameters r and P are gradually increased from their initial values using Equations (11) and (15), respectively, also at every 20 iterations. After that, the iterative procedure is continued until the maximum number of iterations nit_{max} is achieved. For clarity, we use a different nomenclature for each phase of the optimization procedure: (1) parameter increasing phase; (2) stabilization phase. The first phase refers to the continuation procedure, with updates to r , β and P every 20 iterations; we choose $\gamma_r = \left(\frac{r_{max}}{0.01}\right)^{\frac{1}{nit_{min}-1}}$, $\gamma_\beta = \left(\frac{\beta_{max}}{\beta_0}\right)^{\frac{1}{nit_{min}-1}}$ and $\gamma_P = \left(\frac{P_{max}}{P_0}\right)^{\frac{1}{nit_{min}-1}}$, to ensure that r , β and P reach their maximum values exactly in $nit_{min} - 20 = 980$ iterations; then 20 more iterations are performed, completing the parameter increasing phase in $nit_{min} = 1000$ iterations. Then, these parameters are kept constant during 1000 more iterations, i.e., $nit_{max} = 2000$, completing the stabilization phase. Lagrange multipliers (used in Local strategies 1 and 2) and the c_{PM} parameter (used in Global strategies 2, 3 and 4) are updated during the whole optimization process, i.e. during both parameter increase and stabilization phases.

Parameters r_{max} and P_{max} are chosen based on numerical experiments; four values are defined as follows for each solution strategy.

Local 1, 2, 3 and 4. $r_{max} = 10^3, 10^4, 10^5$ and 10^6 .

Global 1. $P_{max} = 50, 100, 300$ and 500 .

Global 2 and 3. $P_{max} = 50, 100, 200$ and 300 .

Global 4. Fixed $P = P_{max} = 50, 60, 80$ and 100 .

All the test problems in the manuscript have been run on a laptop equipped with an Intel(R) Core(TM) i5-7200U CPU @ 2.50GHz, 12 GB of RAM, using the Julia programming language⁵².

Next, the resulting volume fractions, V_f , and maximum stress constraint violations, $\sigma_{max} - 1$, where $\sigma_{max} = \frac{\max\{\sigma_{eq}(\bar{p})\}}{\sigma_y}$, at 2000 iterations, are shown and analyzed for all solution strategies, in order to identify the r_{max} and P_{max} parameters that provide the best compromise between volume fraction and stress response for both mesh sizes simultaneously. The respective volume and stress iteration histories are presented in Appendix D. Subsections 4.1 and 4.2 discuss the performance of the four local and four global strategies, respectively.

4.1 | Discussion: local strategies

Table 1 shows the volume fractions, V_f , and maximum stress constraint violations, $\sigma_{max} - 1$, obtained after $nit_{max} = 2000$ iterations, for all local solution strategies and both mesh sizes.

Analyzing the volume fractions in Table 1, one can verify that larger values of r_{max} result in larger volume fractions, for all local strategies and both mesh sizes. This behavior is in agreement with the AL/EP function definition, Equation (8), in the sense that the larger the value of r the smaller the relative weight of the volume fraction in the objective function, thus leading to results with larger volume fractions.

When analyzing the stress constraint violations in Table 1, it is verified that a larger value of r_{max} does not strictly result in smaller stress constraint violation. When analyzing the EP approaches individually, i.e. Local strategies 3 and 4, there is a clear tendency of maximum stress constraint violation decreasing for increasing values of $r_{max} \in \{10^3, 10^4, 10^5\}$, for both mesh sizes.

TABLE 1 Volume fractions and maximum stress constraint violations after 2000 iterations, for all local strategies and both mesh resolutions. Most appropriate r_{max} parameters are highlighted in bold for each strategy.

Solution strategy	r_{max}	Mesh: 200×200		Mesh: 800×800	
		V_f (%)	$\sigma_{max} - 1$ (%)	V_f (%)	$\sigma_{max} - 1$ (%)
Local 1: AL + SDM	10^3	23.26	1.31	23.34	15.26
	10^4	23.74	0.15	23.95	0.39
	10^5	25.29	0.60	24.68	1.49
	10^6	28.74	0.32	28.01	1.85
Local 2: AL + MMA	10^3	23.27	1.75	22.80	16.78
	10^4	23.53	0.37	23.34	0.34
	10^5	25.43	0.44	24.32	0.61
	10^6	31.17	0.72	29.27	1.52
Local 3: EP + SDM	10^3	22.33	22.95	22.26	39.18
	10^4	23.53	2.24	23.48	13.05
	10^5	24.70	0.47	24.61	0.79
	10^6	27.55	1.19	28.53	0.64
Local 4: EP + MMA	10^3	22.44	21.26	22.14	38.61
	10^4	23.63	2.10	23.35	13.20
	10^5	25.02	0.60	24.45	1.36
	10^6	28.05	0.93	29.51	0.95

Use of a larger $r_{max} = 10^6$, however, does not improve stress constraint feasibility, on the contrary. It is observed, for Local strategies 3 and 4, that the maximum stress constraint violations for $r_{max} = 10^5$ and $r_{max} = 10^6$ are around 1%, for both mesh sizes. In this case, use of the larger $r_{max} = 10^6$ instead of 10^5 leads to virtually the same maximum stress value, but much worse volume fraction behavior. It turns out that $r_{max} = 10^6$ causes the divergence of the optimization procedure (see Appendix D, Figure D3). This behavior is in accordance with the literature^{47,53}, in the sense that as r increases, subproblems become more and more difficult, leading to numerical instabilities. In this work, we use either SDM or MMA to perform the optimization iterations; although computationally cheap, neither is globally convergent to a local minimum point, which in turn may lead to divergence of the procedure as observed in these cases for $r_{max} = 10^6$.

When analyzing the EP results for $r_{max} \in \{10^3, 10^4, 10^5\}$ in Table 1, one can verify that the behavior of the maximum stress constraint violation for r_{max} equal to either 10^3 or 10^4 is mesh dependent, providing larger maximum stress constraint violation for the more refined mesh, unlike what happens for $r_{max} = 10^5$, which provides an almost mesh independent maximum stress constraint violation around 1%, for both mesh sizes.

Based on the above discussion, we choose $r_{max} = 10^5$ as the most suitable parameter to address this problem using the EP method, since a larger value as 10^6 introduces worse volume fraction behavior with no improvement in stress constraint feasibility, and because a smaller value as 10^4 does not provide good stress response for the more refined mesh.

Comparing the maximum stress constraint violations of the AL strategies (Local 1 and 2) with the EP ones (Local 3 and 4), Table 1, for the same r_{max} , one can observe that maximum stresses are lower for the AL approaches for r_{max} equal to either 10^3 or 10^4 . Analyzing the maximum stresses for $r_{max} = 10^4$ and more refined mesh size, one can verify stress constraint violations around 1% for AL, whereas this value is around 13% for EP. This behavior is in accordance with the literature^{47,53}, in the sense that the r parameter needs not be so large in AL strategies, when compared to EP, to provide satisfactory results. When analyzing the AL maximum stress constraint violations for $r_{max} = 10^5$ and 10^6 , one can verify no improvement regarding stress constraint feasibility when compared to $r_{max} = 10^4$, whereas the volume fractions present some deterioration. For $r_{max} = 10^3$, on the other hand, a smaller volume fraction is obtained; however, it comes at the cost of larger stress constraint violation for the more refined mesh size.

Based on the above discussion, we choose $r_{max} = 10^4$ as the most suitable parameter to address this problem using the AL method, since this value is able to provide stress response as good as the one obtained for $r_{max} = 10^5$, for both mesh sizes, with the advantage of lower volume fraction during the final iterations.

Figure 2 shows the optimized topologies and von Mises equivalent stresses after 2000 iterations for the most promising parameters defined above, i.e. $r_{max} = 10^4$ for AL (Local 1 and 2) and 10^5 for EP (Local 3 and 4), for both mesh sizes. Volume fractions, maximum von Mises stresses, constraint violations and gray level indicators are included next to each figure. The gray levels are measured by⁵¹

$$M_{nd} = \frac{\sum_{e=1}^{N_e} 4\bar{\rho}_e (1 - \bar{\rho}_e)}{N_e} \times 100\%. \quad (16)$$

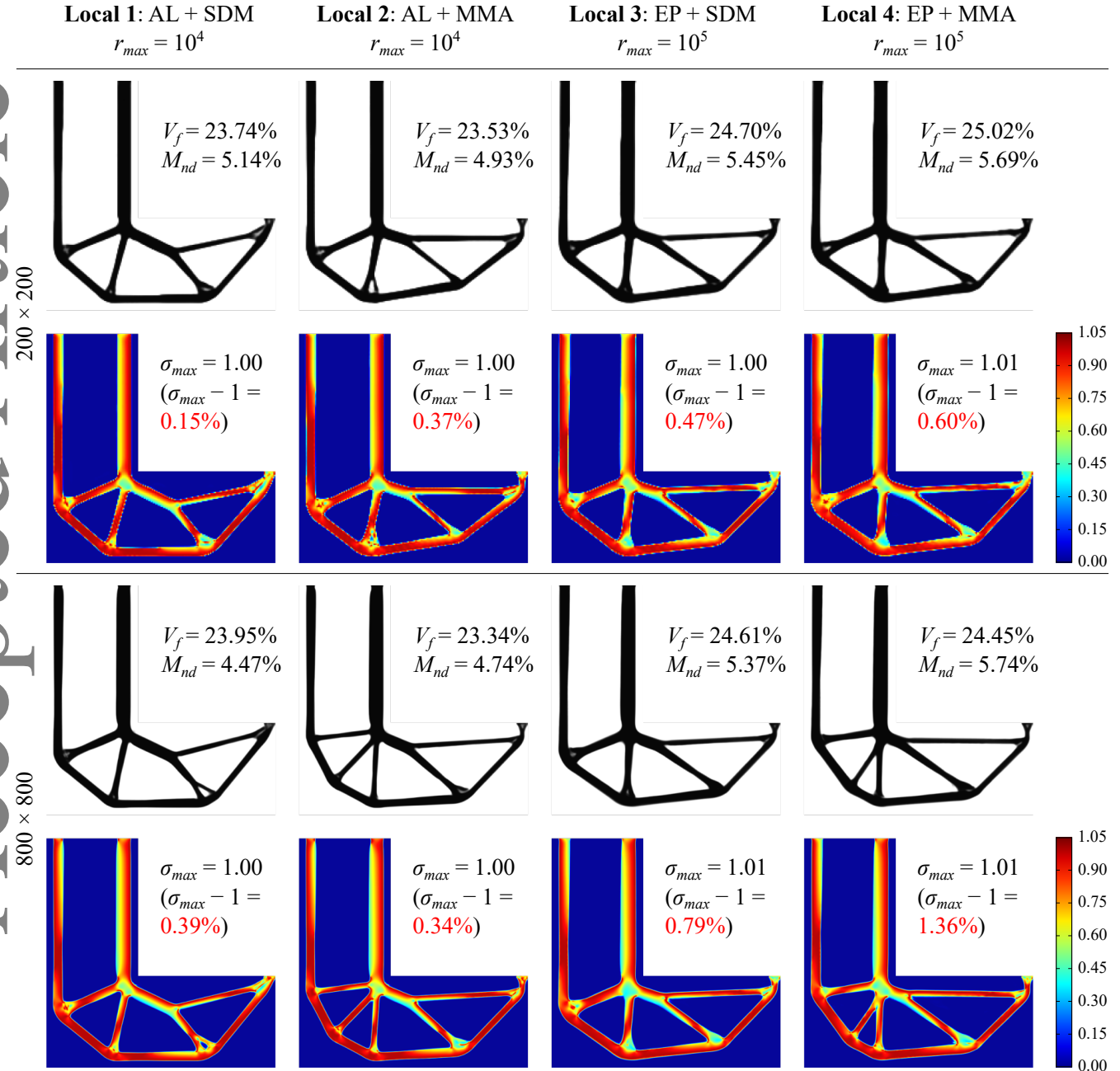


FIGURE 2 Optimized topologies and respective von Mises stresses obtained with the four local strategies for the most promising values of r_{max} and two mesh resolutions, at 2000 iterations.

The relative differences between volume fractions for coarse and fine mesh solutions, given by $\frac{|V_f^{coarse} - V_f^{fine}|}{V_f^{fine}}$, are as follows: 0.88%, 0.81%, 0.37% and 2.33%, for Local strategies 1, 2, 3 and 4, respectively; indicating nearly mesh independent results regarding the volume fraction for all local strategies. When analyzing the optimized topologies, one can verify nearly mesh independent results for the Local 3 strategy (EP + SDM), and also, but slightly worse, for the Local 1 strategy (AL + SDM). When analyzing the Local strategies 2 and 4 (AL + MMA and EP + MMA, respectively), mesh dependent topologies are observed. The differences in the optimized topologies for different mesh sizes are justified: since the stress-constrained optimization problem is highly non-convex, a slight difference between coarse and fine mesh problems, which may occur due to differences in stress accuracy, may lead the iterative procedure to different local minima.

Analyzing Figure 2, it is verified that all results violate the stress constraints by a very small margin. The largest stress constraint violation is 0.60% for the coarse mesh and 1.36% for the fine mesh, both relative to the Local 4 strategy (EP + MMA). The smallest stress constraint violation is 0.15% for the coarse mesh and 0.34% for the fine mesh; these are relative to the Local 1 (AL + SDM) and Local 2 (AL + MMA) strategies, respectively. However, it should be emphasized that these violations do not prevent use of these approaches in practice. As will be demonstrated in subsection 6.1, use of $\alpha < 1$ in the yield stress function, $f_\alpha(\sigma_y)$, works as a simple and effective tool to ensure stress constraint feasibility, at the cost of optimized topologies with slightly larger structural volumes.

4.2 | Discussion: global strategies

Table 2 shows the volume fractions, V_f , and maximum stress constraint violations, $\sigma_{max} - 1$, obtained after $nit_{max} = 2000$ iterations, for all global solution strategies and both mesh sizes.

TABLE 2 Volume fractions and maximum stress constraint violations after 2000 iterations, for all global strategies and both mesh resolutions. Most appropriate P_{max} parameters are highlighted in bold for each strategy.

Solution strategy	P_{max}	Mesh: 200×200		Mesh: 800×800	
		V_f (%)	$\sigma_{max} - 1$ (%)	V_f (%)	$\sigma_{max} - 1$ (%)
Global 1: P -continuation	50	20.72	14.74	20.68	18.86
	100	21.68	6.84	21.80	9.37
	300	22.97	2.52	23.12	2.88
	500	23.89	2.25	24.39	2.12
Global 2: P -continuation + c_{PM} (1 it)	50	24.35	0.00	26.15	0.07
	100	24.23	0.14	25.03	0.09
	200	25.80	0.59	24.90	-0.32
	300	24.40	1.43	27.02	2.75
Global 3: P -continuation + c_{PM} (20 it)	50	24.65	0.01	26.24	0.01
	100	23.86	0.05	25.00	0.04
	200	20.99	154.65	24.46	0.08
	300	24.66	0.19	25.53	0.53
Global 4: Fixed P + c_{PM} (1 it)	50	26.13	-0.01	26.42	0.11
	60	25.44	0.16	25.85	-0.02
	80	27.38	0.12	27.01	0.09
	100	27.55	-0.03	28.04	0.04

Analyzing the maximum stress constraint violations related to the Global 1 strategy (pure P -continuation), Table 2, one can verify that the larger the value of P_{max} the smaller the maximum stress value at 2000 iterations, for both mesh sizes. The volume fractions behave in the opposite way: the larger the value of P_{max} , the larger the volume fraction at 2000 iterations. It turns out, however, that strong oscillations occur for $P_{max} = 500$ during the iterative procedure (see Appendix D, first column of Figures D5 and D6), which is a strong indicator that the optimizer has difficulties to stabilize around some local minimum point at the final iterations when too large P_{max} is employed.

When analyzing the maximum stresses for $P_{max} \in \{50, 100, 300\}$ in Table 2, for the Global 1 strategy, one can verify that the larger the value of P_{max} , the smaller the differences between maximum stresses of coarse and fine mesh results, with little mesh dependence for $P_{max} = 300$.

Based on above observations, it is concluded that $P_{max} = 500$ is not a good choice for the Global 1 strategy, as heavy oscillations occur, preventing the achievement of a local minimum using the MMA implementation employed herein. On the other hand, using smaller values as $P_{max} = 50$ or 100 lead to mesh dependent results regarding the maximum stress value. Hence, $P_{max} = 300$ is the most suitable parameter in this case, since smooth evolution and nearly mesh independent behavior are observed for both volume and maximum stress. Moreover, it is observed that stress constraint violation smaller than 3% is obtained for both mesh sizes, motivating use of a practical approach by employing smaller values of α in the yield stress function to ensure stress constraint feasibility, as demonstrated in subsection 6.1.

Analyzing the maximum stresses of Global strategies 2 and 3 (P -continuation + c_{PM} normalization), Table 2, one can verify near zero stress constraint violation for $P_{max} \in \{50, 100\}$, for both mesh sizes, indicating that use of the adaptive normalization strategy is effective to alleviate the gap between the maximum stress value and the yield stress in these cases. Larger values as $P_{max} = 200$ or 300 , however, lead to strong oscillations during the iterative procedure (see Appendix D, second and third columns of Figures D5 and D6). Using $P_{max} = 200$ leads to numerical instabilities in the coarse mesh problem, whereas $P_{max} = 300$ seems to particularly affect the fine mesh problem. This is justified, since using the c_{PM} adaptive normalization strategy implies non-differentiable stress constraint and hence an additional difficulty to be handled by the optimizer, as discussed in subsection 3.2.1. In these cases, $P_{max} = 200$ or 300 are not attractive anymore, and smaller P_{max} values should be used.

When analyzing the volume fractions for $P_{max} \in \{50, 100\}$, for Global strategies 2 and 3 in Table 2, one can verify that $P_{max} = 100$ provides smaller volume fractions after 2000 iterations. Thus, one can choose $P_{max} = 100$ as the most suitable parameter for Global strategies 2 and 3, since values as large as $P_{max} = 200$ or 300 lead to oscillations during the optimization procedure, and a smaller value of $P_{max} = 50$ leads to worse performance regarding the volume fraction.

When analyzing the volume fractions and maximum stresses related to the Global 4 strategy (Fixed P + c_{PM} normalization) in Table 2, one can verify that $P = 60$ should be employed to achieve the best performance, since it provides near zero stress constraint violation and the smallest volume fraction for both mesh sizes. This is justified, since in this case the value of P is fixed during the whole optimization procedure, i.e. a continuation procedure is not employed. In this case, $P = 80$ or 100 cannot be handled by the optimizer using only 2000 iterations. Moreover, a smaller value of $P = 50$ provides results with worse performance regarding the volume fraction.

Figure 3 shows the optimized topologies and von Mises equivalent stresses after 2000 iterations for the most promising parameters defined above, i.e. $P_{max} = 300$ for P -continuation (Global 1), $P_{max} = 100$ for P -continuation + c_{PM} normalization (Global 2 and 3), and $P = 60$ for fixed P + c_{PM} normalization (Global 4), for both mesh sizes. Volume fractions, maximum von Mises stresses, constraint violations and gray level indicators are included next to each figure.

The relative differences between volume fractions for coarse and fine mesh solutions, given by $\frac{|V_f^{coarse} - V_f^{fine}|}{V_f^{fine}}$, are as follows: 0.65%, 3.20%, 4.56% and 1.59%, for Global strategies 1, 2, 3 and 4, respectively; indicating nearly mesh independent results regarding the volume fraction for all global strategies. When analyzing the optimized topologies, one can verify nearly mesh independent results for Global 1 (P -continuation) and Global 2 (P -continuation + c_{PM} normalization 1 it) strategies. Global 3 (P -continuation + c_{PM} normalization 20 it) and Global 4 (fixed P + c_{PM} normalization 1 it) strategies provide results with different topologies for different mesh sizes.

Analyzing Figure 3, it is verified that the results obtained with Global 1 strategy slightly violate the stress constraint by: 2.52% (coarse mesh result) and 2.88% (fine mesh result). The results obtained with Global strategies 2, 3 and 4 present much better behavior regarding stress feasibility; among these, maximum stress constraint violations for coarse and fine mesh results are 0.16% and 0.09%, respectively, related to Global strategies 4 and 2, respectively. The improvement in stress response comes from use of the adaptive normalization scheme by updates to c_{PM} during the iterative procedure. This approach allows use of Global strategies 2, 3 and 4 without further manipulation to ensure stress constraint feasibility, since $\sigma_{max} \leq 1$ is achieved during the stabilization phase for both mesh sizes, hence allowing imposition of practical stopping criteria without resorting to numerical tolerances regarding the yield stress value.

5 | STRESS CONSTRAINT FEASIBILITY AND STOPPING CRITERIA

We employ the following criteria to stop the iterative procedure and accept the current topology as the optimized solution:

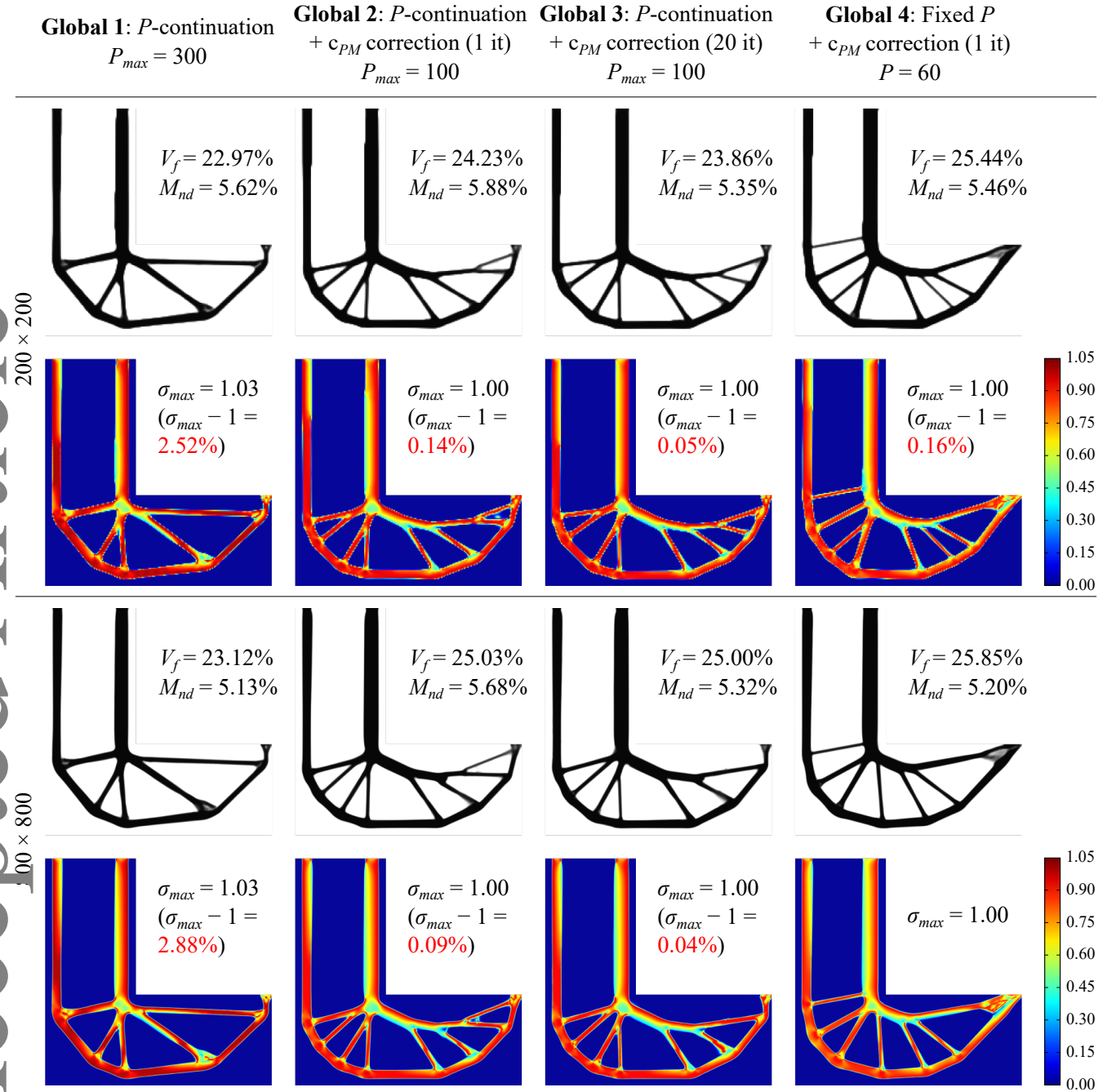


FIGURE 3 Optimized topologies and respective von Mises stresses obtained with the four global strategies for the most promising values of P_{max} and two mesh resolutions, at 2000 iterations.

- Stabilization criterion: $\|\Delta\rho\|_{\infty} \leq 0.01$;
- Feasibility criterion: $\sigma_{max} - 1 \leq 0$;

otherwise, the procedure is interrupted when the maximum number of iterations, nit_{max} , is reached.

In order to check for the ability to meet the stabilization criterion, one can analyze evolution of the maximum change between two consecutive iterations, $\|\Delta\rho\|_{\infty}$. These are shown in Figure 4 for the most promising r_{max} and P_{max} values, as determined in the parametric study, section 4, for all local and global solution strategies, considering the 800×800 mesh resolution.

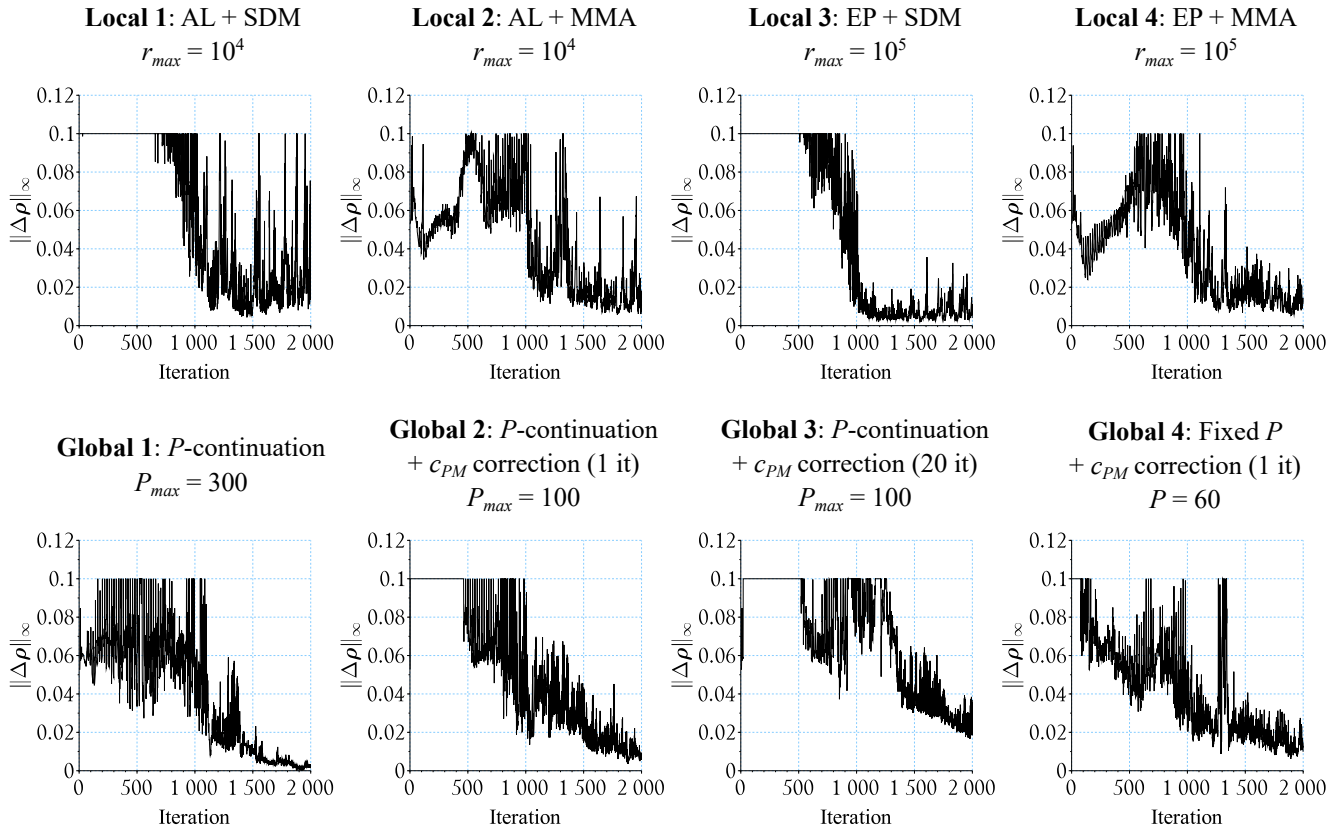


FIGURE 4 Maximum change iteration histories for all local and global solution strategies, for the most promising values of r_{max} and P_{max} , respectively, and 800×800 mesh size.

Local strategies 3 and 4 and all global strategies present a maximum change that gradually diminishes during the stabilization phase (Iteration > 1000), indicating that these can satisfy the stabilization criterion without further manipulation. The Local 1 strategy, on the other hand, presents some strong oscillations at the stabilization phase, in which $\|\Delta\rho\|_\infty$ reaches its maximum value several times. Some oscillations are also observed in the maximum change graph related to Local 2 strategy. Thus, it is concluded that Local strategies 1 and 2 require some manipulation to enforce stabilization of the optimization procedure, as proposed in subsection 5.2.

Regarding the ability to meet the feasibility criterion, it is observed that the Global strategies 2, 3 and 4 are able to achieve stress constraint feasibility during the stabilization phase for both mesh sizes, i.e. $\sigma_{max} - 1 \leq 0$, as shown in Figure 5 for the fine mesh problem with greater emphasis on the stabilization phase. All local and Global 1 strategies cannot provide stress constraint feasibility without considering some tolerance on the yield stress value, requiring some manipulation to ensure stress constraint feasibility, as proposed in subsections 5.1 and 5.2.

5.1 | Exterior Penalty and pure P -continuation strategies

EP-based methods iterate through the unfeasible region; as $r \rightarrow \infty$, the solution of the subproblem tends to the solution of the original problem⁵³. However, when analyzing the EP-based strategies proposed herein (Local 3 and 4), it was shown that a large value of $r = 10^6$ causes divergence of the iterative procedure, forcing use of $r_{max} = 10^5$, meaning that some strategy is required to ensure constraint feasibility. The same applies for the pure P -continuation strategy based on the P -mean function (Global 1), since it underestimates the maximum stress value for finite P .

In order to achieve stress constraint feasibility when using either EP-based or pure P -continuation strategies, we propose to employ $\alpha < 1$ in the yield stress function. When analyzing the maximum von Mises stress iteration histories of Local 3, Local 4 and Global 1 strategies in Figure 5, it is verified that most oscillations occur within a tolerance of 2% on the yield stress function

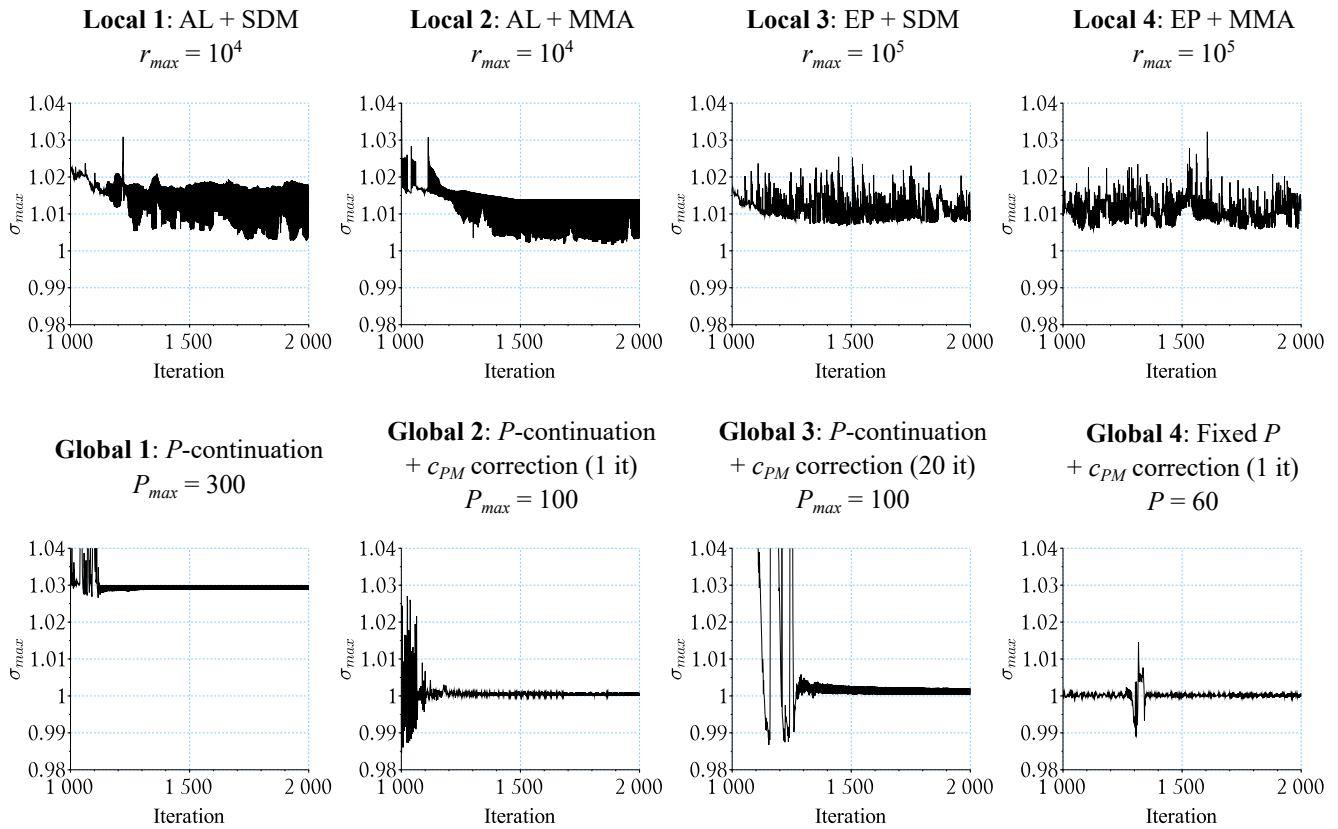


FIGURE 5 Maximum von Mises stresses for all local and global solution strategies, for the most promising values of r_{max} and P_{max} , respectively, and 800×800 mesh size.

for Local strategies 3 and 4, and 3% for the Global 1 strategy. Thus, based on this observation, we choose $\alpha = 0.98$ for Local strategies 3 and 4, and $\alpha = 0.97$ for the Global 1.

5.2 | Augmented Lagrangian strategies

In AL-based methods, there is no need for r to go to infinity to achieve the solution of the original problem^{47,53}. The proposed AL-based strategies (Local 1 and 2), however, were not able to reach a feasible point during the iterative procedure. This is justified, since achievement of the stationary point of each subproblem is not ensured, and none of the optimization methods employed to solve the subproblems are globally convergent to a local minimum point.

In order to achieve stress constraint feasibility when using the AL-based strategies proposed herein, one can use the same approach as proposed for the EP-based and P -continuation strategies, with $\alpha = 0.98$, since most oscillations occur within a 2% tolerance range when using $r_{max} = 10^4$, Figure 5. However, special attention should be given to the oscillations in the maximum change at the stabilization phase, Figure 4 (Local 1 and 2), which are not alleviated by ensuring stress constraint feasibility.

Figure 6 shows the maximum change graphs of Local 1 (AL + SDM) and Local 3 (EP + SDM) strategies for $r_{max} = 10^3$, 10^4 and 10^5 , for the fine mesh problem. Analyzing the maximum change graphs related to the AL-based strategy, Figure 6 (first row), it can be seen that the oscillations are stronger for $r_{max} = 10^3$, and tend to diminish for $r_{max} = 10^5$. Analyzing the graphs related to the EP-based strategy, Figure 6 (second row), it can be seen that the maximum change tends to stabilize for all r_{max} values considered, indicating that these oscillations are due to the use of the AL method in association with small r_{max} values, and are not related to the solution strategy of the optimization subproblems, since the same method is employed in AL and EP strategies. Since the only difference between AL and EP strategies is that in the former the Lagrange multipliers are updated every 20 iterations, it can be concluded that the oscillations are due to the updates of the Lagrange multipliers during the stabilization phase.

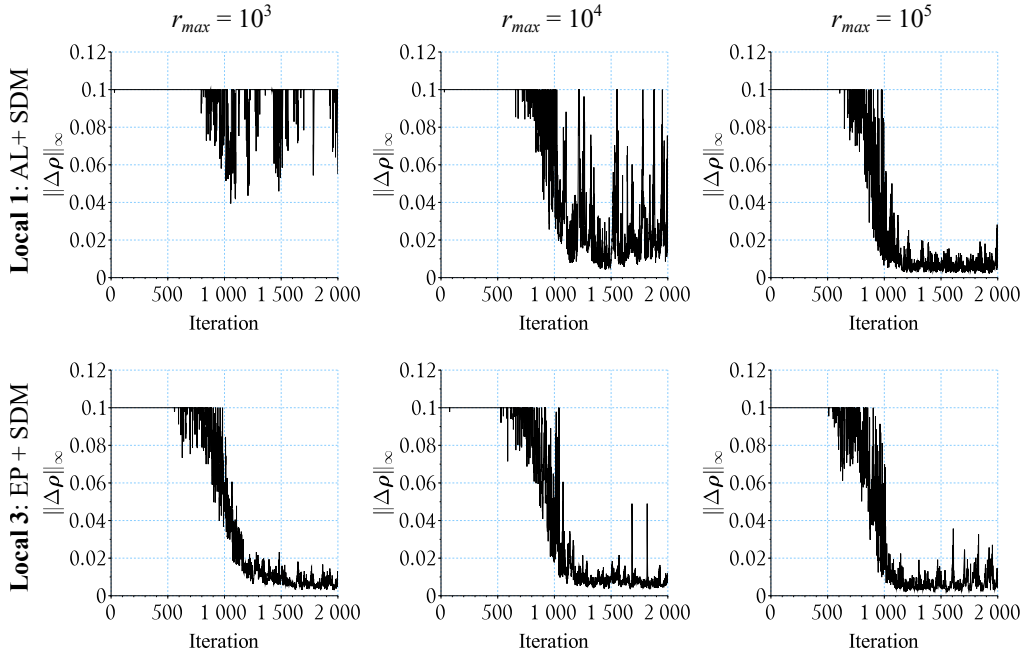


FIGURE 6 Maximum change iteration histories of Local strategies 1 and 3 for three different values of r_{max} , 800×800 mesh size.

Based on the above observations, we propose an alternative procedure to perform the optimization iterations when using the AL-based strategies. The parameter increasing phase is carried out normally, with updates to μ and r every 20 iterations until nit_{min} iterations are completed. In this first phase, the value of r is increased up to $r_{max}^{(1)} = 10^4$, which is the most promising r_{max} parameter for the AL-based strategies determined in section 4. The stabilization phase, on the other hand, is carried out using a different strategy: first, a larger maximum penalization parameter is defined, $r_{max}^{(2)}$; then, the iterative procedure is performed with updates to r and μ every 20 iterations only if $\sigma_{max} > 1$. The upper bound $r_{max}^{(2)} = 10^5$ is chosen, since it allows process stabilization even with updates to μ every 20 iterations, Figure 6, and it is not large enough to cause divergence of the procedure (see subsection 4.1). When using this strategy in association with $\alpha = 0.98$, stress constraint feasibility and process stabilization are simultaneously achieved, making the AL-based approaches able to meet the practical stopping criteria employed herein.

Use of the proposed approach provides some flexibility on the choice of parameter α . If α is sufficiently small, there is no need to update the Lagrange multipliers at all, since these are updated during the stabilization phase only if $\sigma_{max} > 1$; in this case, the Lagrange multipliers are kept constant after the parameter increasing phase is finished, hence allowing stabilization of $\|\Delta\rho\|_\infty$ during the final iterations. On the other hand, if α is too large (which may happen since it may be problem-dependent), the Lagrange multipliers will be constantly updated since σ_{max} will constantly be larger than 1 during the stabilization phase, thus a larger upper bound of $r_{max}^{(2)} = 10^5$ becomes important, in the sense that using such a large value of r allows stabilization of the procedure even though the Lagrange multipliers are updated every 20 iterations, Figure 6. In order to update r during the stabilization phase, Equation (11) is applied using $\gamma_r = \sqrt[4]{10}$, hence ensuring a minimum of 80 iterations to reach $r = r_{max}^{(2)}$.

5.3 | Summary of approaches and best parameters

The values of α to be applied in the yield stress function, $f_\alpha(\sigma_y)$, and the most promising r_{max} and P_{max} parameters for all local and global strategies, respectively, are listed below.

Local 1 and 2. $\alpha = 0.98$, $r_{max}^{(1)} = 10^4$ and $r_{max}^{(2)} = 10^5$. During the stabilization phase, μ and r are updated each 20 iterations only if $\sigma_{max} > 1$.

Local 3 and 4. $\alpha = 0.98$ and $r_{max} = 10^5$.

Global 1. $\alpha = 0.97$ and $P_{max} = 300$.

Global 2 and 3. $\alpha = 1.00$ and $P_{max} = 100$.

Global 4. $\alpha = 1.00$ and $P = 60$.

These parameters are employed to address the problems in the results section.

6 | RESULTS AND DISCUSSION

6.1 | Sensitivity to the aggressiveness of the continuation procedure

In this section, a high-resolution version of the L-shaped problem is addressed. The feasibility and stabilization stopping criteria and best parameters defined in section 5 are employed. The problem is solved for the 800×800 mesh resolution with each of the eight solution strategies, for four different values of nit_{min} : 200, 500, 800 and 1000; resulting in 32 optimization problems. The maximum number of iterations $nit_{max} = 2000$ used in the parametric study is employed for all cases.

Figures 7 and 8 show the optimized topologies and respective von Mises equivalent stress fields obtained with the four local solution strategies. Table 3 summarizes the main outcomes from the local strategies results.

TABLE 3 Volume fractions, maximum stress constraint violations, number of iterations, and run times for the cases in Figures 7 and 8, obtained with the four local strategies.

Solution strategy	nit_{min}	V_f (%)	$\sigma_{max} - 1$ (%)	Iterations	Run time (h)
Local 1: AL + SDM	200	25.41	-1.23	317	0.8
	500	24.80	-0.39	605	1.5
	800	24.80	-0.38	861	1.9
	1000	24.64	-0.39	1046	2.2
Local 2: AL + MMA	200	25.55	-1.02	626	2.0
	500	24.17	-0.45	644	1.6
	800	24.00	-0.28	1205	3.1
	1000	24.07	-0.57	1133	2.6
Local 3: EP + SDM	200	26.42	-1.37	372	1.1
	500	25.33	-0.54	541	1.3
	800	25.06	-0.20	816	1.8
	1000	24.97	-0.31	1038	2.3
Local 4: EP + MMA	200	26.25	-0.64	747	2.3
	500	25.36	-0.96	744	2.0
	800	25.07	-0.48	956	2.1
	1000	24.91	-1.14	1181	2.8

Analyzing Figure 7 (second, third and four rows), related to the local strategies, one can verify that all topologies for $nit_{min} \in \{500, 800, 1000\}$ are sharp and well defined, presenting few gray regions other than the transition boundaries between solid and void phases. The same applies to the topologies obtained with Local strategies 1, 2 and 3 for $nit_{min} = 200$, Figure 7 (first row; first, second and third columns). Analyzing the topology obtained with the Local 4 strategy for $nit_{min} = 200$, Figure 7 (first row, fourth column), gray regions inside the structural members are verified, indicating numerical instabilities during the optimization procedure. This is confirmed by the number of iterations to achieve the stopping criteria: 747 for $nit_{min} = 200$ against 744 for $nit_{min} = 500$, i.e. 547 iterations are performed during the stabilization phase for $nit_{min} = 200$, whereas this number is 244 for $nit_{min} = 500$, indicating that use of $nit_{min} = 200$ imposes difficulties to meet the stopping criteria during the stabilization phase; hence also indicating that, in this case, 200 iterations are not sufficient to perform the continuation procedure.

In addition, all local strategies are very flexible regarding the number of iterations to perform the continuation procedure, nit_{min} . The parametric study and choice of best parameters (r_{max} , P_{max} and α) addressed in sections 4 and 5 were performed for $nit_{min} = 1000$. It can be seen that most local approaches continue to work well for nit_{min} values as small as 200, Figure 7 (first

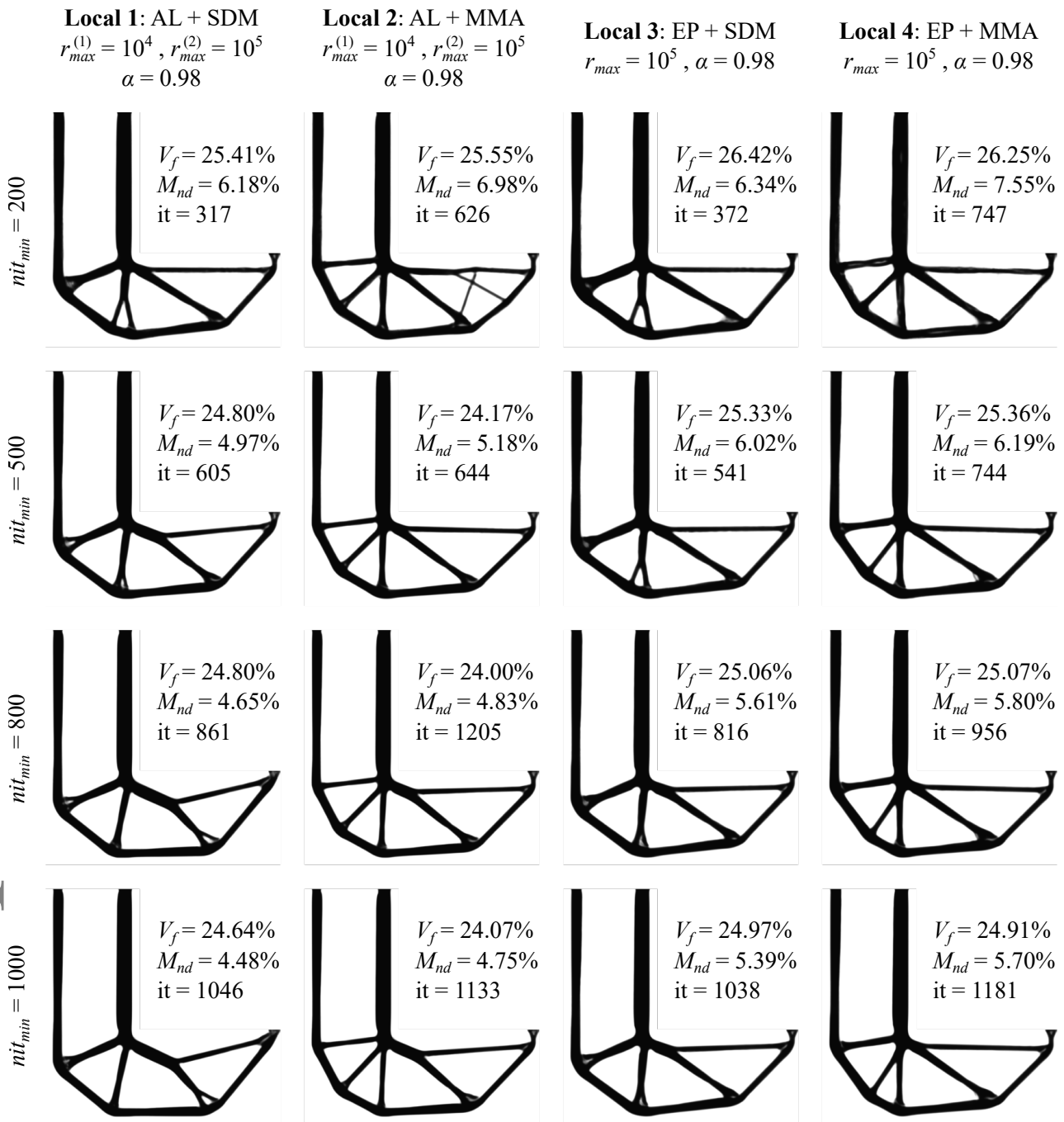


FIGURE 7 Optimized topologies obtained with the four local strategies using stabilization and feasibility stopping criteria, 800×800 mesh size.

row), still providing very promising results. Thus, it is verified that the local strategies addressed herein are quite stable and are not very sensitive to the choice of nit_{min} within the range of parameters analyzed. Special attention is given to the AL-based strategies (Local 1 and 2), which present an almost nit_{min} -independent volume fraction for $nit_{min} \in \{500, 800, 1000\}$, Table 3, in addition to providing the smallest volume fractions among all local strategies.

It can be observed, in Table 3, that all results related to the local strategies satisfy the stress constraint at the end of the iterative procedure; thus, all approaches are compared regarding volume fraction only. Among the local approaches, we choose the Local 2 strategy (AL + MMA) as the most promising one, since it provides the smallest volume fraction, $V_f = 24.00\%$, as shown in

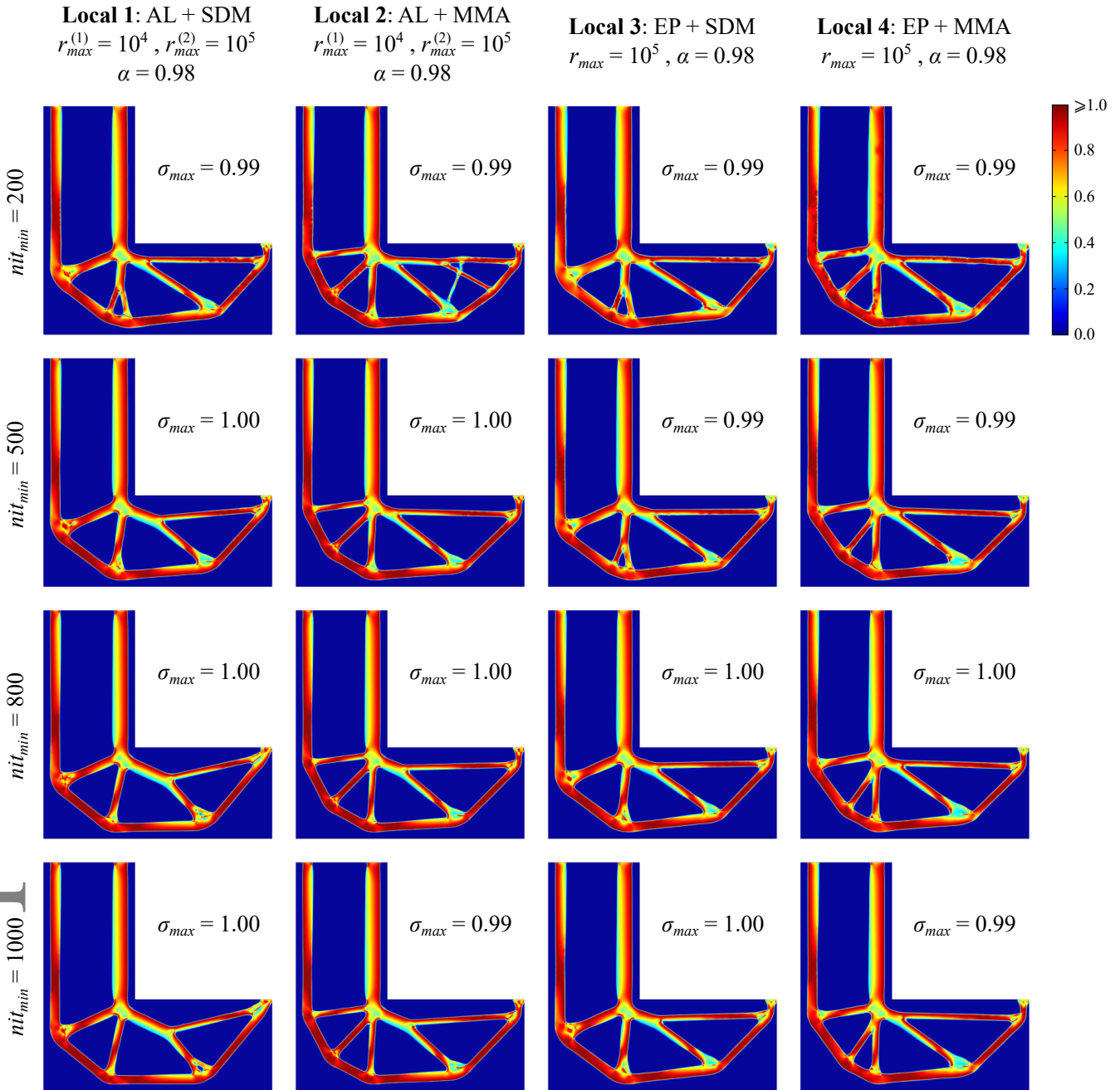


FIGURE 8 Von Mises equivalent stresses of topologies from Figure 7.

Table 3. Regarding the computational effort, it can be seen that the SDM-based methods, i.e. Local 1 and 3, tend to achieve the stopping criteria using a smaller number of iterations when compared to the MMA-based counterparts (Local 2 and 4). This improvement in the number of iterations, however, seems to sacrifice performance of the AL-based strategy a little, in which the smallest volume fraction obtained with use of SDM (i.e., Local 1) is 24.64%, Table 3. When comparing SDM and MMA in the EP-based strategies (i.e. Local 3 and 4), almost identical volume fractions are verified for the same nit_{min} , Table 3, indicating that SDM is more appropriate in this case, since the optimized solution is achieved using less iterations.

Figures 9 and 10 show the optimized topologies and respective von Mises equivalent stress fields obtained with the four global solution strategies. Table 4 summarizes the main outcomes from the global strategies results.

Analyzing Figure 9 (fourth row), related to the global strategies, it is verified that all topologies for $nit_{min} = 1000$ are very sharp and well defined. For $nit_{min} = 800$, Global 1 strategy provides a topology with some deterioration and gray regions,

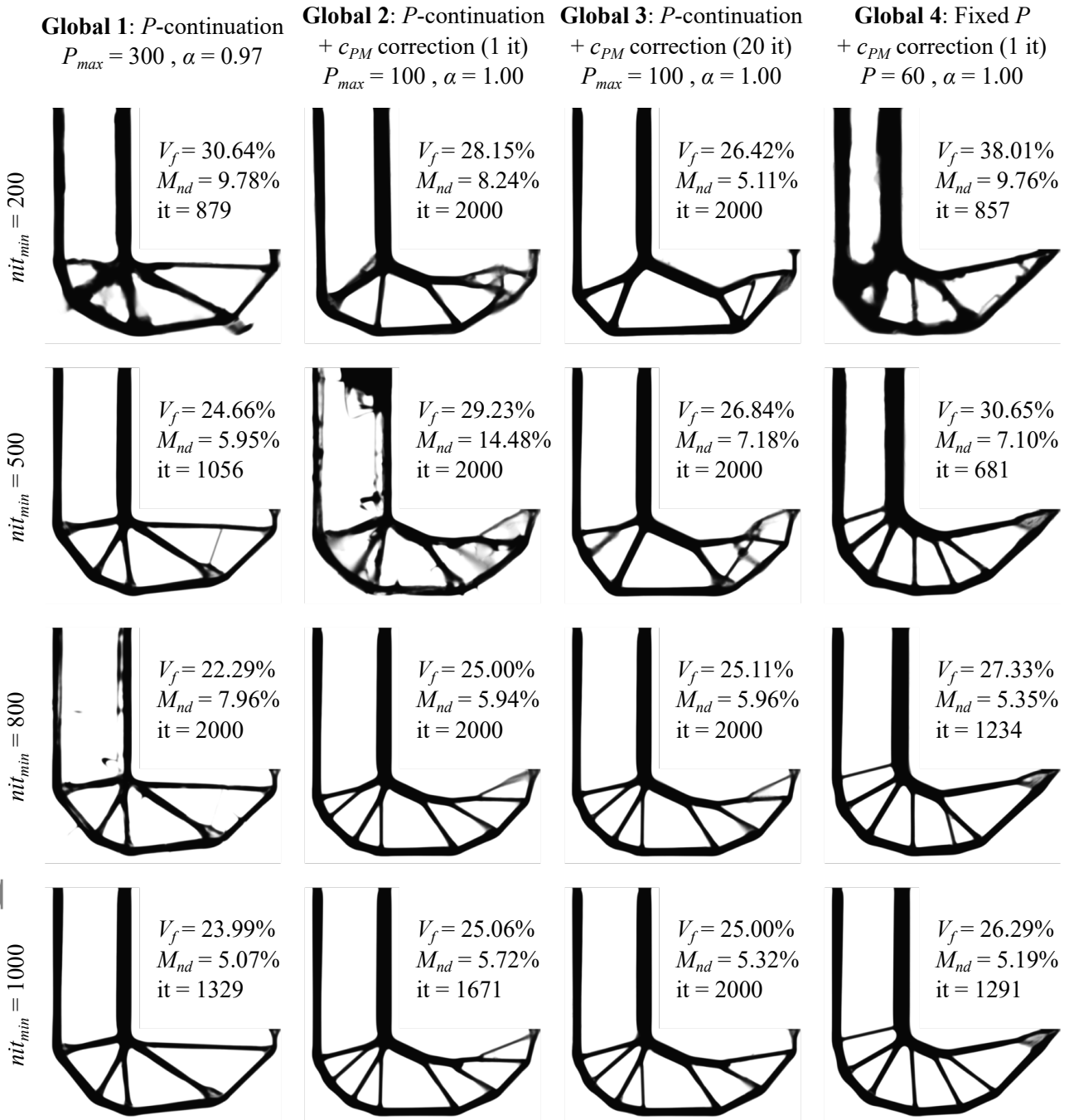


FIGURE 9 Optimized topologies obtained with the four global strategies using stabilization and feasibility stopping criteria, 800×800 mesh size.

which cannot be used in practice, Figure 9 (third row, first column). When analyzing the corresponding von Mises stress field in Figure 10, stress constraint violation around 63% is observed, indicating the optimizer faces difficulties to achieve the feasibility criterion during the iterative procedure. The same is observed for the Global 2 strategy and $nit_{min} = 500$: a severely deteriorated topology with too much gray that cannot be used in practice is achieved, with stress constraint violation around 52%, as shown in Figures 9 and 10 (second row, second column). Some deterioration is also observed in topologies obtained with Global strategies 1 and 4 and $nit_{min} = 200$, Figure 9 (first row; first and fourth columns); however, in these cases, the results meet the feasibility criterion. Nevertheless, these topologies should not be used in practice, since some regions are disconnected and too much gray

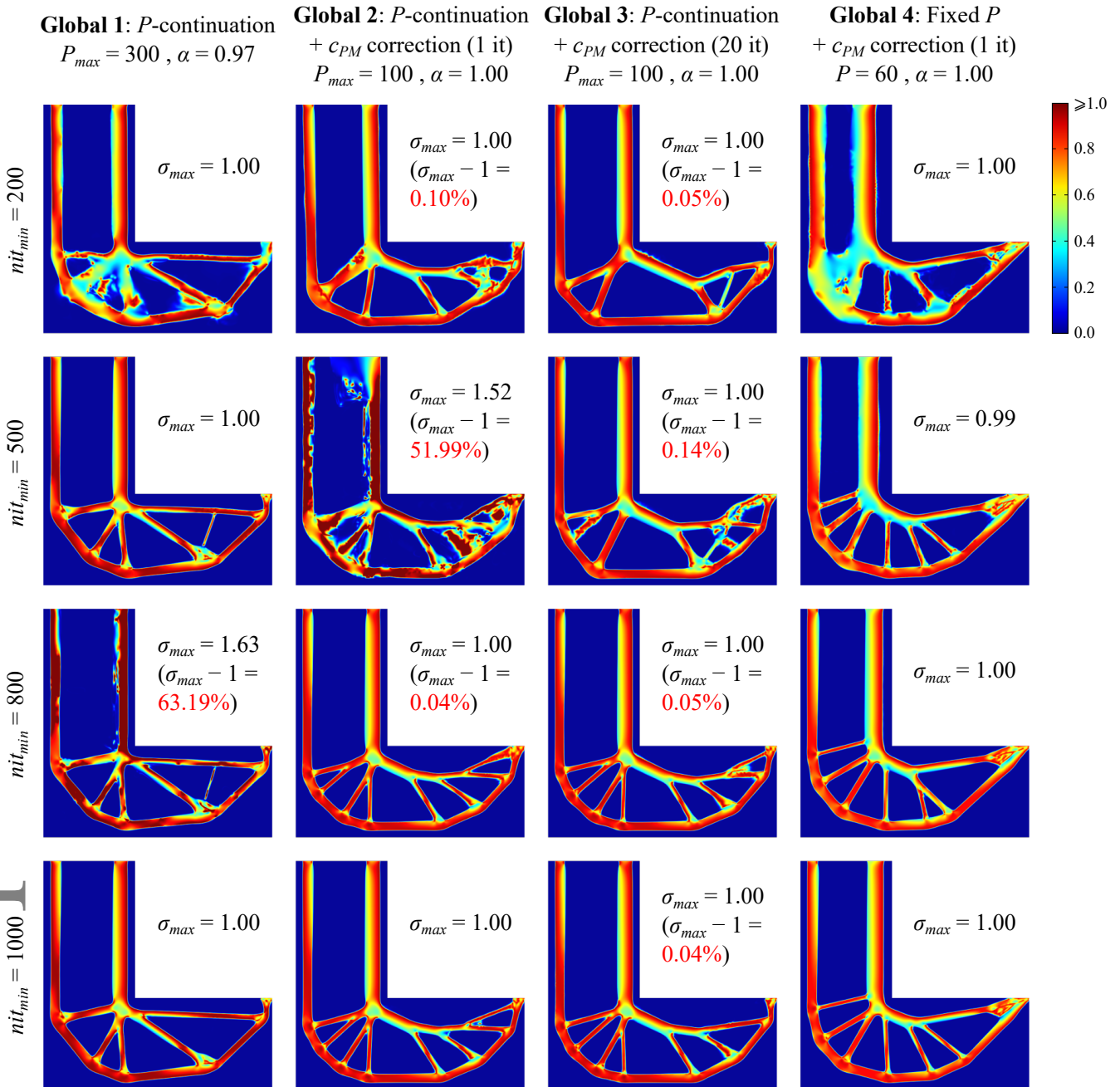


FIGURE 10 Von Mises equivalent stresses of topologies from Figure 9.

is observed, mainly at the result relative to the Global 1 strategy. Based on the above, it is verified that the global strategies are more sensitive to the choice of nit_{min} ; the only approach that presents satisfactory topologies for all values of nit_{min} is the Global 3 strategy, Figure 9 (third column), although some gray regions are verified in the topology for $nit_{min} = 500$.

Analyzing the von Mises stresses obtained using the global strategies, Table 4, one can verify that two results present large stress constraint violations: Global 1 for $nit_{min} = 800$ and Global 2 for $nit_{min} = 500$. The other results either satisfy the stress constraint at all points or present small stress constraint violations ($< 0.2\%$), indicating that the c_{PM} update strategy may benefit from use of $\alpha < 1$ in the yield stress function, a result to be confirmed in future studies. Analyzing Table 4, it is verified that the stopping criteria are not met in several problems, indicating that more iterations are necessary in the parameters increasing and/or stabilization phases. The only approach that meets the stopping criteria for the four nit_{min} considered is the Global 4 strategy.

TABLE 4 Volume fractions, maximum stress constraint violations, number of iterations, and run times for the cases in Figures 9 and 10, obtained with the four global strategies.

Solution strategy	nit_{min}	V_f (%)	$\sigma_{max} - 1$ (%)	Iterations	Run time (h)
Global 1: P -continuation	200	30.64	-0.03	879	2.8
	500	24.66	-0.05	1056	3.7
	800	22.29	63.19	2000	11.3
	1000	23.99	-0.15	1329	3.8
Global 2: P -continuation + c_{PM} (1 it)	200	28.15	0.10	2000	6.4
	500	29.23	51.99	2000	7.7
	800	25.00	0.04	2000	5.8
	1000	25.06	0.00	1671	4.7
Global 3: P -continuation + c_{PM} (20 it)	200	26.42	0.05	2000	6.6
	500	26.84	0.14	2000	6.4
	800	25.11	0.05	2000	6.0
	1000	25.00	0.04	2000	5.9
Global 4: Fixed P + c_{PM} (1 it)	200	38.01	-0.10	857	2.8
	500	30.65	-0.80	681	2.0
	800	27.33	-0.05	1234	3.6
	1000	26.29	-0.26	1291	3.5

When analyzing the topologies obtained with the global strategies regarding objective, we choose the Global 1 strategy (pure P -continuation) as the most promising one, since it provides the smallest volume fraction, $V_f = 23.99\%$, among the results that satisfy the stress constraint, as shown in Table 4. However, it seems that this strategy is very sensitive to the choice of nit_{min} , since unusable topologies are achieved for $nit_{min} = 200$ and 800 , Figure 9 (first column). This is justified, since $P = 300$ is reached at the final steps of the continuation procedure, leading to a very nonlinear optimization problem and difficulties regarding convergence. When comparing the Global 1 result for $nit_{min} = 1000$, Figure 9 (fourth row, first column), with the Local 2 result for $nit_{min} = 800$, Figure 7 (third row, second column), one can verify identical topologies and almost identical volume fractions. However, using the Local 2 strategy provides flexibility in the choice of nit_{min} , allowing one to obtain a similar solution with almost identical volume fraction, within a much smaller number of iterations, as observed for $nit_{min} = 500$, Figure 7 (second row, second column), in which 644 iterations are performed and a volume fraction of 24.17% is achieved.

Figure 11 shows the volume fractions of the optimized topologies obtained with all local and global strategies with respect to nit_{min} , Figures 7 and 9, respectively. In these graphs, the two results that violate the stress constraint the most are highlighted, both related to the global strategies. The other stress constraint violations ($< 0.2\%$), also related to the global strategies, are omitted. Analyzing Figure 11 for $nit_{min} = 1000$, one can verify that the volume fractions of all local strategies are between the volume fractions of Global 1 (bottom) and Global 2 and 3 (top) strategies, i.e. crudely speaking, it can be said that the local strategies addressed herein have a performance that is similar to the global strategies for P_{max} values between 100 and 300. The Local 2 strategy (AL + MMA) provides a volume fraction very similar to the one obtained with the Global 1 strategy for $P_{max} = 300$. The EP-based strategies (Local 3 and 4), on the other hand, provide volume fractions very similar to the ones obtained with Global strategies 2 and 3 with $P_{max} = 100$. The Local 1 strategy (AL + SDM) provides a result slightly better than Global strategies 2 and 3 regarding volume fraction, but it is worse than the Global 1.

When analyzing Figure 11 for $nit_{min} \in \{200, 500, 800\}$, one can verify that the volume graphs related to the Global strategies 1, 2 and 3 oscillate, whereas all graphs related to the local approaches remain smooth and tend to stabilize as nit_{min} increases, indicating that more iterations are required to couple the global strategies with such large values as $P_{max} = 100$ or 300 , even when a continuation procedure is employed, as done herein. The only global strategy that presents smooth behavior and seems to stabilize as nit_{min} increases is the Global 4 approach, which is run for a fixed value of $P = 60$; however, the obtained results are worse in performance when compared to all local strategies, specially when a more aggressive continuation approach is performed, as observed for smaller values of nit_{min} .

Analyzing the results for $nit_{min} = 1000$ in Tables 3 and 4, one can verify that the local strategies require less iterations to meet the stopping criteria when compared to the global ones. The differences in the number of iterations are even greater for

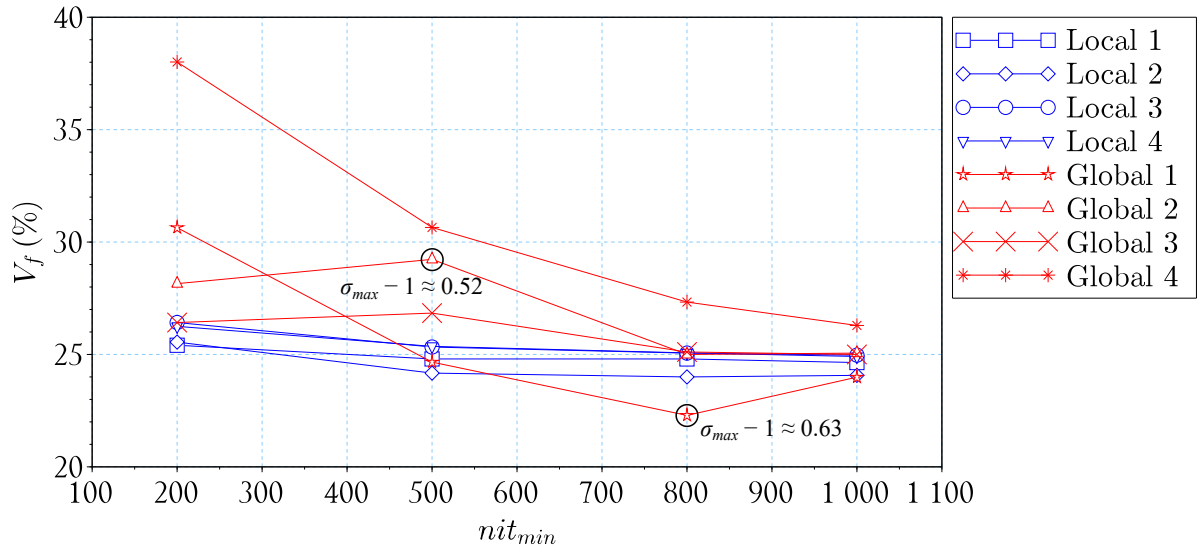


FIGURE 11 Volume fractions of optimized topologies from Figures 7 and 9 with respect to nit_{min} . Points with extreme stress constraint violation are indicated in the graphs: Global 1 for $nit_{min} = 800$ and Global 2 for $nit_{min} = 500$.

smaller values of nit_{min} . It is verified that the global approaches require a slower and more careful continuation procedure when large values of P are employed; thus, reducing the value of nit_{min} imposes much difficulty to the optimizer and prevents it from meeting the stopping criteria in some cases, leading the algorithm to reaching the maximum number of iterations.

6.2 | High-resolution verification

In order to demonstrate the generality of the results, in this section we apply our findings to a different design problem, i.e. the crack design²¹, Figure 12 (A), where also the mesh resolution is increased significantly. With symmetry conditions employed, the half domain is discretized by 1600×3200 ($N_e = 5,120,000$), Figure 12 (B). The same input data employed for the L-shaped problem are used in this case, with the exception of $\beta_{max} \cong \frac{R}{l_c \sqrt{3}} \cong 55.426$. The total applied load is distributed over a boundary length of 0.025.

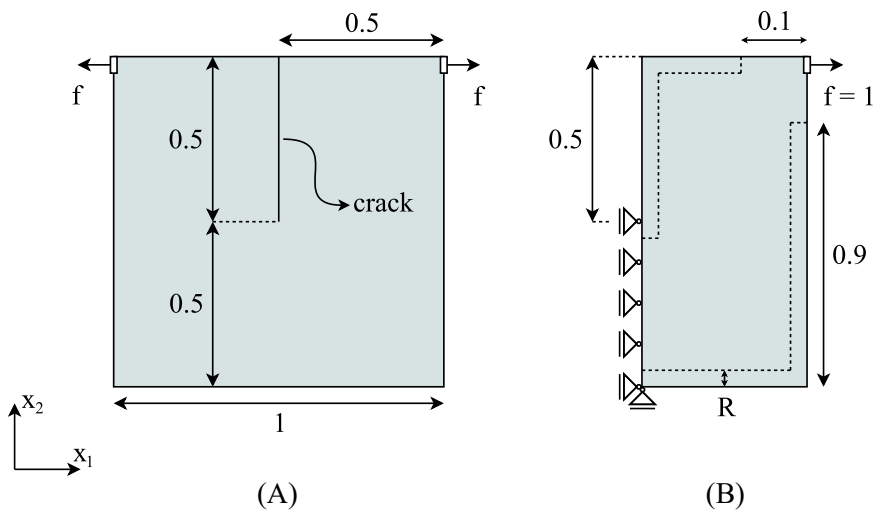


FIGURE 12 (A) Crack problem and (B) design domain employed in optimization (exploiting symmetry). The padding region is represented by dashed lines.

The optimization problem is solved using the Local 1 and Global 4 strategies, for $nit_{min} = 500$. These strategies are chosen based on the computational efficiency demonstrated in subsection 6.1. The Global 4 strategy is the only global approach that reached an acceptable design in less than 1000 iterations, Figure 9, which makes it attractive for large-scale problems. The Local 1 strategy was found to be the most promising AL-based strategy regarding efficiency, Figure 7.

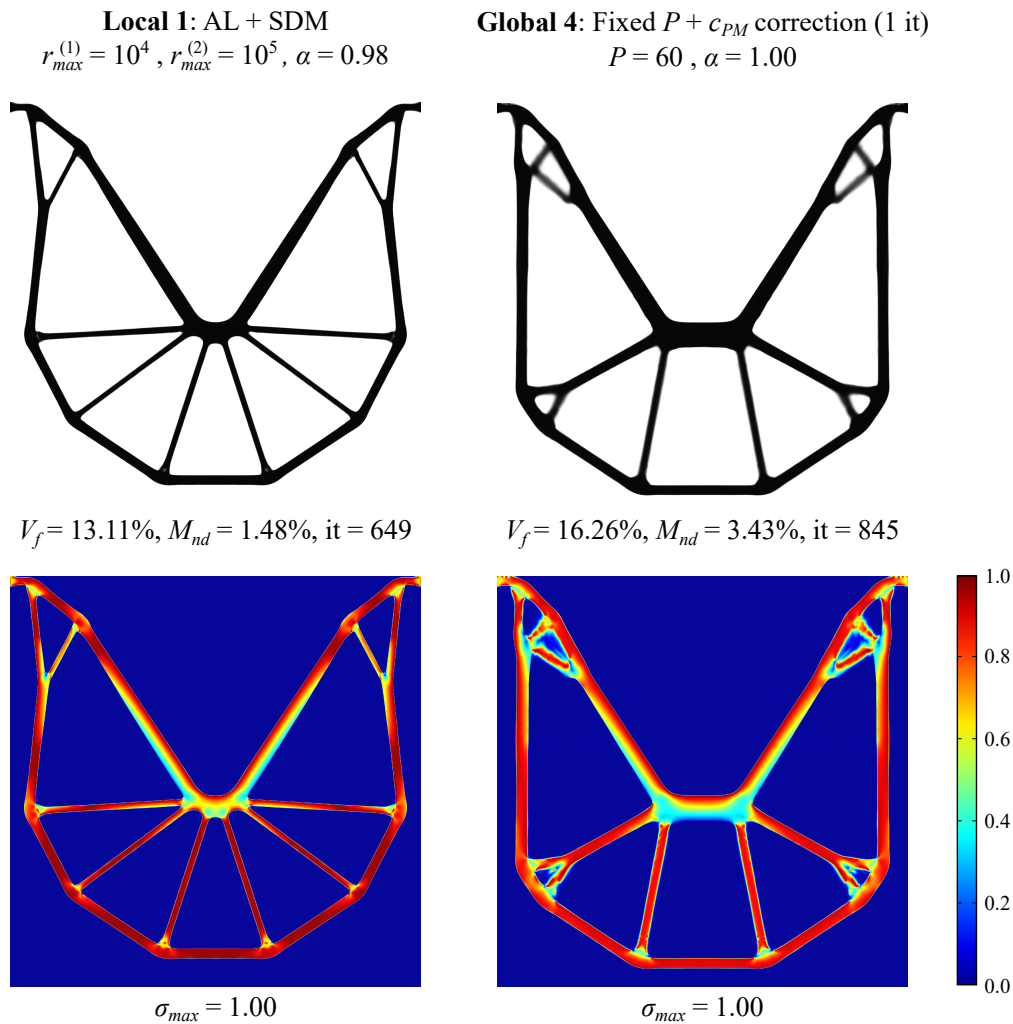


FIGURE 13 Crack problem. Optimized topologies and respective von Mises stress fields obtained with Local 1 (left) and Global 4 (right) strategies, for $nit_{min} = 500$. Half domain resolution: 1600×3200 ($N_e = 5,120,000$).

Figure 13 shows the optimized topologies and respective von Mises stress fields. Analyzing Figure 13, it is observed that the Local 1 strategy reached an optimized topology in less iterations and with smaller volume fraction when compared to the Global 4 strategy result, confirming the results shown in subsection 6.1. Besides, the topology obtained with the Global 4 strategy presents blurred structural members next to the region where the loads are applied, unlike the Local 1 strategy result, which has well-defined structural members. Moreover, the structural members of the Global 4 strategy result have few points close to the yield stress value, which is a strong indicator that its structural volume could be further minimized while keeping the stress constraint satisfied. This example confirms prior observations thereby demonstrating that these also hold for alternative design settings and large-scale problems.

7 | DISCUSSION AND CONCLUDING REMARKS

This work has proposed and investigated eight solution strategies to address stress-constrained topology optimization. The volume minimization problem with stress constraint has been addressed from two different viewpoints: (1) local stress-constrained formulation; and (2) global stress-constrained formulation. Four local and four global strategies have been considered: the local strategies are based on either the Augmented Lagrangian (AL) or the pure Exterior Penalty (EP) method; the global strategies are based on the standard P -mean aggregation function. The following final remarks can be drawn:

1. All local and global strategies can achieve topologies with nearly mesh independent volume fractions, provided that large enough values of r_{max} or P_{max} are employed, respectively.
2. In order to ensure stress constraint feasibility in all local strategies and in the pure P -continuation global strategy, use of an easily defined reduction factor on the yield stress value is necessary. Use of the adaptive normalization scheme on the global strategy allows the achievement of stress constraint feasibility without resorting to reduction factors.
3. When using a large number of iterations to run the parameter increasing phase (continuation procedure), it was verified that the local strategies are comparable to the global ones regarding optimized volume fraction, provided that the global strategies are run with values of P between 100 and 300. The EP-based local strategies provide similar results to the global ones for $P_{max} = 100$, whereas the AL-based local strategy, when coupled with MMA to solve the subproblems, provides a similar result to the pure P -continuation strategy for $P_{max} = 300$. The AL-based local strategy coupled with SDM provides a better result than the EP-based strategies, but worse than the MMA-based AL counterpart.
4. The local strategies are less sensitive to the number of iterations employed to perform the parameter increasing phase, allowing more aggressive procedures; hence, also obtaining optimized topologies in less iterations. The global strategies are more sensitive to the continuation procedure, specially when large values as $P_{max} = 100$ or 300 are employed, resulting in divergence of the procedure when the number of iterations for the continuation approach is not suitable. Use of a fixed $P = 60$ in the global approach provides more flexibility in reducing the number of iterations spent in the continuation procedure, at the cost of a larger number of iterations in the stabilization phase and worse results when compared to the local strategies.

The final remarks were drawn based on the P -mean function. In a smaller side study, we have investigated four other aggregation functions: P -norm, lower bound KS, upper bound KS⁷; and Heaviside aggregation⁴⁵ (see Appendix C). The conclusions regarding better efficiency of the local strategies also apply for these cases. The global strategies may also be employed, however a more careful continuation procedure should be carried out, associated with large values of P_{max} , like $P_{max} \geq 100$, to achieve results at the level of those provided by the local approaches.

Based on results presented herein, we conclude that stress-constrained topology optimization should be addressed by local strategies. The AL-based strategies (Local 1 and 2) are very promising and should be preferable over global ones, since they provide better efficiency and performance for medium- and large-scale problems.

ACKNOWLEDGMENTS

G. A. da Silva and A. T. Beck kindly acknowledge financial support of this research project by the agencies FAPESP (São Paulo Research Foundation), grant number 2018/16701-1, and CNPq (National Council for Research and Development), grant number 309107/2020-2. This study was financed in part by the Coordination for the Improvement of Higher Education Personnel - Brazil (CAPES) - Finance Code 001. N. Aage and O. Sigmund were supported by the Villum Investigator Project InnoTop funded by the Villum Foundation.

DATA AVAILABILITY STATEMENT

All data required to reproduce results in this study are included in the paper.

References

1. Svanberg K. The method of moving asymptotes - a new method for structural optimization. *International Journal for Numerical Methods in Engineering* 1987; 24(2): 359 - 373. doi: 10.1002/nme.1620240207
2. Duysinx P, Bendsøe MP. Topology optimization of continuum structures with local stress constraints. *International Journal for Numerical Methods in Engineering* 1998; 43(8): 1453 - 1478. doi: 10.1002/(SICI)1097-0207(19981230)43:8<1453::AID-NME480>3.0.CO;2-2
3. Le C, Norato J, Bruns T, Ha C, Tortorelli D. Stress-based topology optimization for continua. *Structural and Multidisciplinary Optimization* 2010; 41(4): 605 - 620. doi: 10.1007/s00158-009-0440-y
4. Svärd H. Interior value extrapolation: a new method for stress evaluation during topology optimization. *Structural and Multidisciplinary Optimization* 2015; 51(3): 613 - 629. doi: 10.1007/s00158-014-1171-2
5. da Silva GA, Beck AT, Sigmund O. Stress-constrained topology optimization considering uniform manufacturing uncertainties. *Computer Methods in Applied Mechanics and Engineering* 2019; 344: 512 - 537. doi: 10.1016/j.cma.2018.10.020
6. Duysinx P, Sigmund O. New developments in handling stress constraints in optimal material distribution. In: Paper presented at: Proceedings of the 7th AIAA/USAF/NASA/ISSMO Symposium on Multidisciplinary Analysis and Optimization. ; 1998; St. Louis, MO: 1501 - 1509
7. Verbart A, Langelaar M, Keulen vF. A unified aggregation and relaxation approach for stress-constrained topology optimization. *Structural and Multidisciplinary Optimization* 2017; 55: 663-679. doi: 10.1007/s00158-016-1524-0
8. París J, Navarrina F, Colominas I, Casteleiro M. Block aggregation of stress constraints in topology optimization of structures. *Advances in Engineering Software* 2010; 41(3): 433 - 441. doi: 10.1016/j.advengsoft.2009.03.006
9. Holmberg E, Torstenfelt B, Klarbring A. Stress constrained topology optimization. *Structural and Multidisciplinary Optimization* 2013; 48(1): 33–47. doi: 10.1007/s00158-012-0880-7
10. Fancello EA, Pereira JT. Structural topology optimization considering material failure constraints and multiple load conditions. *Latin American Journal of Solids and Structures* 2003; 1(1): 3 - 24.
11. Pereira JT, Fancello EA, Barcellos CS. Topology optimization of continuum structures with material failure constraints. *Structural and Multidisciplinary Optimization* 2004; 26(1-2): 50 - 66. doi: 10.1007/s00158-003-0301-z
12. Fancello EA. Topology optimization for minimum mass design considering local failure constraints and contact boundary conditions. *Structural and Multidisciplinary Optimization* 2006; 32(3): 229 - 240. doi: 10.1007/s00158-006-0019-9
13. da Silva GA, Cardoso EL. Stress-based topology optimization of continuum structures under uncertainties. *Computer Methods in Applied Mechanics and Engineering* 2017; 313: 647 - 672. doi: 10.1016/j.cma.2016.09.049
14. da Silva GA, Beck AT, Sigmund O. Topology optimization of compliant mechanisms with stress constraints and manufacturing error robustness. *Computer Methods in Applied Mechanics and Engineering* 2019; 354: 397 - 421. doi: 10.1016/j.cma.2019.05.046
15. da Silva GA, Cardoso EL, Beck AT. Comparison of robust, reliability-based and non-probabilistic topology optimization under uncertain loads and stress constraints. *Probabilistic Engineering Mechanics* 2020; 59: 103039. doi: 10.1016/j.probenmech.2020.103039
16. da Silva GA, Beck AT, Sigmund O. Topology optimization of compliant mechanisms considering stress constraints, manufacturing uncertainty and geometric nonlinearity. *Computer Methods in Applied Mechanics and Engineering* 2020; 365: 112972. doi: 10.1016/j.cma.2020.112972
17. Giraldo-Londoño O, Paulino GH. A unified approach for topology optimization with local stress constraints considering various failure criteria: von Mises, Drucker-Prager, Tresca, Mohr-Coulomb, Bresler-Pister and Willam-Warnke. *Proc. R. Soc. A* 2020; 476: 20190861. doi: 10.1098/rspa.2019.0861

18. Senhora FV, Giraldo-Londoño O, Menezes IFM, Paulino GH. Topology optimization with local stress constraints: a stress aggregation-free approach. *Structural and Multidisciplinary Optimization* 2020; 62: 1639-1668. doi: 10.1007/s00158-020-02573-9
19. Giraldo-Londoño O, Paulino GH. PolyStress: a Matlab implementation for local stress-constrained topology optimization using the augmented Lagrangian method. *Structural and Multidisciplinary Optimization* 2021. doi: 10.1007/s00158-020-02760-8
20. Emmendoerfer H, Fancello EA. A level set approach for topology optimization with local stress constraints. *International Journal for Numerical Methods in Engineering* 2014; 99(2): 129 - 156. doi: 10.1002/nme.4676
21. Emmendoerfer H, Fancello EA. Topology optimization with local stress constraint based on level set evolution via reaction-diffusion. *Computer Methods in Applied Mechanics and Engineering* 2016; 305: 62 - 88. doi: 10.1016/j.cma.2016.02.024
22. Emmendoerfer H, Silva ECN, Fancello EA. Stress-constrained level set topology optimization for design-dependent pressure load problems. *Computer Methods in Applied Mechanics and Engineering* 2019; 344: 569 - 601. doi: 10.1016/j.cma.2018.10.004
23. Emmendoerfer H, Fancello EA, Silva ECN. Stress-constrained level set topology optimization for compliant mechanisms. *Computer Methods in Applied Mechanics and Engineering* 2020; 362: 112777. doi: 10.1016/j.cma.2019.112777
24. da Silva GA, Aage N, Beck AT, Sigmund O. Three-dimensional manufacturing tolerant topology optimization with hundreds of millions of local stress constraints. *International Journal for Numerical Methods in Engineering* 2021; 122: 548-578. doi: 10.1002/nme.6548
25. Fernández E, Collet M, Alarcón P, Bauduin S, Duysinx P. An aggregation strategy of maximum size constraints in density-based topology optimization. *Structural and Multidisciplinary Optimization* 2019; 60: 2113-2130. doi: 10.1007/s00158-019-02313-8
26. París J, Navarrina F, Colominas I, Casteleiro M. Topology optimization of continuum structures with local and global stress constraints. *Structural and Multidisciplinary Optimization* 2009; 39(4): 419 - 437. doi: 10.1007/s00158-008-0336-2
27. de Assis Pereira A, Cardoso EL. On the influence of local and global stress constraint and filtering radius on the design of hinge-free compliant mechanisms. *Structural and Multidisciplinary Optimization* 2018; 58(2): 641 - 655. doi: 10.1007/s00158-018-1915-5
28. Bendsøe MP, Sigmund O. *Topology Optimization: Theory, Methods and Applications*. Berlin: Springer . 2004
29. da Silva GA, Beck AT, Cardoso EL. Topology optimization of continuum structures with stress constraints and uncertainties in loading. *International Journal for Numerical Methods in Engineering* 2018; 113(1): 153 - 178. doi: 10.1002/nme.5607
30. Bruggi M, Duysinx P. Topology optimization for minimum weight with compliance and stress constraints. *Structural and Multidisciplinary Optimization* 2012; 46(3): 369–384. doi: 10.1007/s00158-012-0759-7
31. Sigmund O, Maute K. Topology optimization approaches. *Structural and Multidisciplinary Optimization* 2013; 48(6): 1031 - 1055. doi: 10.1007/s00158-013-0978-6
32. Bathe KJ. *Finite Element Procedures*. Upper Saddle River, New Jersey: Prentice Hall . 1996.
33. Amir O, Aage N, Lazarov BS. On multigrid-CG for efficient topology optimization. *Structural and Multidisciplinary Optimization* 2014; 49: 815 - 829. doi: 10.1007/s00158-013-1015-5
34. Cheng GD, Guo X. ϵ -relaxed approach in structural topology optimization. *Structural Optimization* 1997; 13(4): 258 - 266. doi: 10.1007/BF01197454
35. Wang F, Lazarov BS, Sigmund O. On projection methods, convergence and robust formulations in topology optimization. *Structural and Multidisciplinary Optimization* 2011; 43(6): 767–784. doi: 10.1007/s00158-010-0602-y

36. Lazarov BS, Sigmund O. Filters in topology optimization based on Helmholtz-type differential equations. *International Journal for Numerical Methods in Engineering* 2011; 86: 765-781. doi: 10.1002/nme.3072
37. Luo Y, Kang Z. Topology optimization of continuum structures with Drucker-Prager yield stress constraints. *Computers & Structures* 2012; 90-91: 65 - 75. doi: 10.1016/j.compstruc.2011.10.008
38. Luo Y, Wang MY, Kang Z. An enhanced aggregation method for topology optimization with local stress constraints. *Computer Methods in Applied Mechanics and Engineering* 2013; 254: 31 - 41. doi: 10.1016/j.cma.2012.10.019
39. Moon SJ, Yoon GH. A newly developed qp-relaxation method for element connectivity parameterization to achieve stress-based topology optimization for geometrically nonlinear structures. *Computer Methods in Applied Mechanics and Engineering* 2013; 265: 226 - 241. doi: 10.1016/j.cma.2013.07.001
40. de Leon DM, Alexandersen J, O. Fonseca JS, Sigmund O. Stress-constrained topology optimization for compliant mechanism design. *Structural and Multidisciplinary Optimization* 2015; 52(5): 929 - 943. doi: 10.1007/s00158-015-1279-z
41. Kiyono C, Vatanabe S, Silva E, Reddy J. A new multi-p-norm formulation approach for stress-based topology optimization design. *Composite Structures* 2016; 156: 10 - 19. doi: 10.1016/j.compstruct.2016.05.058
42. Zhang S, Gain AL, Norato JA. Stress-based topology optimization with discrete geometric components. *Computer Methods in Applied Mechanics and Engineering* 2017; 325: 1 - 21. doi: <https://doi.org/10.1016/j.cma.2017.06.025>
43. Picelli R, Townsend S, Brampton C, Norato J, Kim H. Stress-based shape and topology optimization with the level set method. *Computer Methods in Applied Mechanics and Engineering* 2018; 329: 1 - 23. doi: <https://doi.org/10.1016/j.cma.2017.09.001>
44. Sharma A, Maute K. Stress-based topology optimization using spatial gradient stabilized XFEM. *Structural and Multidisciplinary Optimization* 2018; 57: 17-38. doi: 10.1007/s00158-017-1833-y
45. Wang C, Qian X. Heaviside projection-based aggregation in stress-constrained topology optimization. *International Journal for Numerical Methods in Engineering* 2018; 115(7): 849-871. doi: 10.1002/nme.5828
46. Leader MK, Chin TW, Kennedy GJ. High-Resolution Topology Optimization with Stress and Natural Frequency Constraints. *AIAA Journal* 2019; 57(8): 3562-3578. doi: 10.2514/1.J057777
47. Birgin EG, Martínez JM. *Practical Augmented Lagrangian Methods for Constrained Optimization*. Philadelphia, PA: Society for Industrial and Applied Mathematics . 2014
48. Aage N, Lazarov BS. Parallel framework for topology optimization using the method of moving asymptotes. *Structural and Multidisciplinary Optimization* 2013; 47: 493-505. doi: 10.1007/s00158-012-0869-2
49. Yang D, Liu H, Zhang W, Li S. Stress-constrained topology optimization based on maximum stress measures. *Computers and Structures* 2018; 198: 23 - 39. doi: 10.1016/j.compstruc.2018.01.008
50. Lee E, James KA, Martins JRR. Stress-constrained topology optimization with design-dependent loading. *Structural and Multidisciplinary Optimization* 2012; 46: 647 - 661. doi: 10.1007/s00158-012-0780-x
51. Sigmund O. Morphology-based black and white filters for topology optimization. *Structural and Multidisciplinary Optimization* 2007; 33(4-5): 401 - 424. doi: 10.1007/s00158-006-0087-x
52. Bezanson J, Edelman A, Karpinski S, Shah VB. Julia: A fresh approach to numerical computing. *SIAM review* 2017; 59(1): 65-98. doi: 10.1137/141000671
53. Arora JS. *Introduction to Optimum Design*. Boston: Academic Press. 3rd ed. 2012.
54. Aage N, Andreassen E, Lazarov BS. Topology optimization using PETS: An easy-to-use, fully parallel, open source topology optimization framework. *Structural and Multidisciplinary Optimization* 2015; 51: 565-572. doi: 10.1007/s00158-014-1157-0

55. Andreassen E, Clausen A, Schevenels M, Lazarov BS, Sigmund O. Efficient topology optimization in MATLAB using 88 lines of code. *Structural and Multidisciplinary Optimization* 2011; 43: 1 - 16. doi: 10.1007/s00158-010-0594-7



APPENDIX

A SOLVING THE OPTIMIZATION SUBPROBLEMS

Given that the equilibrium constraint is automatically satisfied after solving the state problem, Equation (9), only bound constraints are left to be handled by the optimizer. In this paper, two numerical optimization methods are adopted to solve the Augmented Lagrangian (AL) and pure Exterior Penalty (EP) subproblems: the Steepest Descent method with Move limits (SDM)^{24,29} and the Method of Moving Asymptotes (MMA)¹; both are general mathematical programming tools able to handle bound constraints.

The SDM update scheme is described in Appendix D of reference²⁴; it is repeated here for the sake of completeness. The MMA update scheme follows the implementation by Aage et al.⁵⁴ with modifications to the move limits and asymptotes computation. The iteration framework is given as follows in three steps; steps 1 and 2 are shared by both approaches, while step 3 is approach specific. Since we are handling bound constraints only, step 3 of MMA can be written in closed form¹⁹.

1. *Sensitivity analysis.* Given the design variables at iteration b , written as $\boldsymbol{\rho}^{(b)}$, compute the gradient of the AL (or EP) function, $\mathbf{G} = \nabla_{\boldsymbol{\rho}} L \Big|_{\boldsymbol{\rho}=\boldsymbol{\rho}^{(b)}}$, using the adjoint method (see Appendix B.1).
2. *Set move limits.* Lower, $\boldsymbol{\rho}^{inf}$, and upper, $\boldsymbol{\rho}^{sup}$, move limits are set based on two previous iterations, by using the auxiliary variable $d_e = (\rho_e^{(b)} - \rho_e^{(b-1)}) \times (\rho_e^{(b-1)} - \rho_e^{(b-2)})$, as

$$\delta_e = \begin{cases} \max \{0.7\delta_e, 0.001\} & \text{if } d_e < 0 \\ \min \{1.1\delta_e, 0.1\} & \text{if } d_e > 0 \end{cases} \quad (\text{A1})$$

$$\begin{aligned} \rho_e^{inf} &= \rho_e^{(b)} - \delta_e \\ \rho_e^{sup} &= \rho_e^{(b)} + \delta_e \end{aligned}$$

where δ_e is an auxiliary variable employed to compute the lower, ρ_e^{inf} , and upper, ρ_e^{sup} , move limits associated with the e -th design variable. The optimization procedure is started with maximum range of move limits, i.e. $\delta_e = 0.1$, and these are updated from the third iteration.

3. *Update design variables.* Compute $\boldsymbol{\rho}^{(b+1)}$ using either SDM or MMA.
 - 3.1. SDM

- (a) Reset the gradient contributions at the bound constraints, as

$$\mathbf{G}_e^{new} = \begin{cases} 0 & \text{if } \rho_e^{(b)} = 1 \text{ and } G_e < 0 \\ 0 & \text{if } \rho_e^{(b)} = 0 \text{ and } G_e > 0 \\ G_e & \text{otherwise} \end{cases} \quad (\text{A2})$$

- (b) Compute $\boldsymbol{\rho}^{(b+1)}$ using unitary step length $\Psi = 1$, as

$$\rho_e^{(b+1)} = \max \left\{ 0, \max \left\{ \rho_e^{inf}, \min \left\{ 1, \min \left\{ \rho_e^{sup}, \rho_e^{(b)} - \Psi \frac{G_e^{new}}{\|\mathbf{G}^{new}\|_{\infty}} \right\} \right\} \right\} \right\}. \quad (\text{A3})$$

3.2. MMA

- (a) Compute lower, $\bar{\mathbf{L}}$, and upper, $\bar{\mathbf{U}}$, asymptotes, as

$$\begin{aligned} \bar{L}_e &= \rho_e^{(b)} - 0.2 \\ \bar{U}_e &= \rho_e^{(b)} + 0.2 \end{aligned} \quad (\text{A4})$$

(b) Compute lower, $\bar{\alpha}$, and upper, $\bar{\beta}$, bounds to the design variables, as

$$\begin{aligned}\bar{\alpha}_e &= \max \left\{ \max \left\{ \rho_e^{inf}, 0 \right\}, 0.9\bar{L}_e + 0.1\rho_e^{(b)} \right\} \\ \bar{\beta}_e &= \min \left\{ \min \left\{ \rho_e^{sup}, 1 \right\}, 0.9\bar{U}_e + 0.1\rho_e^{(b)} \right\}\end{aligned}\quad (A5)$$

(c) Compute the auxiliary variables \mathbf{p}_0 and \mathbf{q}_0 , as

$$\begin{aligned}p_{0e} &= \left(\bar{U}_e - \rho_e^{(b)} \right)^2 \left(\max \left\{ 0, G_e \right\} + 0.001 |G_e| + \frac{0.5 \cdot 10^{-6}}{\bar{U}_e - \bar{L}_e} \right) \\ q_{0e} &= \left(\rho_e^{(b)} - \bar{L}_e \right)^2 \left(\max \left\{ 0, -G_e \right\} + 0.001 |G_e| + \frac{0.5 \cdot 10^{-6}}{\bar{U}_e - \bar{L}_e} \right)\end{aligned}\quad (A6)$$

(d) Compute $\rho^{(b+1)}$ by applying the bounds on the closed form solution, as

$$\rho_e^{(b+1)} = \max \left\{ \bar{\alpha}_e, \min \left\{ \bar{\beta}_e, \frac{\bar{L}_e \sqrt{p_{0e}} + \bar{U}_e \sqrt{q_{0e}}}{\sqrt{p_{0e}} + \sqrt{q_{0e}}} \right\} \right\}.\quad (A7)$$

The main difference between the standard MMA implementation and the current one is on the computation of move limits and asymptotes. Instead of considering outer move limits of fixed size, the update scheme of Equation (A1) is employed, as also considered for the SDM; thus, a fairer comparison is performed, since the SDM and MMA approaches differ in the update rule only, as shown in step 3. The asymptotes, on the other hand, are computed based on the rule of fixed size, Equation (A4), which was defined based on numerical experiments, unlike the standard MMA implementation where these are continuously updated based on two previous iterations.

B SENSITIVITY ANALYSIS

B.1 Augmented Lagrangian and pure Exterior Penalty

The adjoint method is used to compute the derivative of the AL (or EP) function with respect to a physical relative density $\bar{\rho}_n$. The AL function, Equation (8), is rewritten as

$$L = V_f(\bar{\rho}) + \frac{r}{2} \sum_{k=1}^{N_k} \left\langle \frac{\mu_k}{r} + \frac{\sigma_{eq}^{(k)}(\bar{\rho})}{f_\alpha(\sigma_y)} - 1 \right\rangle^2 + \lambda^T (\mathbf{K}(\bar{\rho}) \mathbf{U}(\bar{\rho}) - \mathbf{F}),\quad (B8)$$

where λ is the adjoint vector, which is arbitrary, since $\mathbf{K}(\bar{\rho}) \mathbf{U}(\bar{\rho}) - \mathbf{F} = \mathbf{0}$. The derivative of Equation (B8) is shown in detail by da Silva et al.⁵ and is given by

$$\frac{\partial L}{\partial \bar{\rho}_n} = \frac{\partial V_f(\bar{\rho})}{\partial \bar{\rho}_n} + h_n \frac{\partial f_\sigma(\bar{\rho}_n)}{\partial \bar{\rho}_n} \hat{\sigma}_{eq}^{(n)}(\bar{\rho}) + \lambda_n^T \frac{\partial \mathbf{k}_n(\bar{\rho}_n)}{\partial \bar{\rho}_n} \mathbf{u}_n(\bar{\rho}),\quad (B9)$$

where

$$\frac{\partial V_f(\bar{\rho})}{\partial \bar{\rho}_n} = \frac{V_n}{\sum_{e=1}^{N_e} V_e}\quad (B10)$$

is the derivative of the volume fraction,

$$\frac{\partial f_\sigma(\bar{\rho}_n)}{\partial \bar{\rho}_n} = \frac{\varepsilon}{[\varepsilon(1 - \bar{\rho}_n) + \bar{\rho}_n]^2}\quad (B11)$$

is the derivative of the stress interpolation function,

$$\frac{\partial \mathbf{k}_n(\bar{\rho}_n)}{\partial \bar{\rho}_n} = (1 - \rho_{min}) p \bar{\rho}_n^{p-1} \mathbf{k}_n^0\quad (B12)$$

is the derivative of the stiffness matrix, and

$$h_n = \left\langle \mu_n + r \left(\frac{\sigma_{eq}^{(n)}(\bar{\rho})}{f_\alpha(\sigma_y)} - 1 \right) \right\rangle \frac{1}{f_\alpha(\sigma_y)}.\quad (B13)$$

The local adjoint vector is computed as $\lambda_n = \mathbf{H}_n \lambda$, where \mathbf{H}_n is the localization operator³². The global adjoint vector is obtained by solving the following system of linear equations

$$\mathbf{K}(\bar{\rho}) \lambda = - \sum_{k=1}^{N_k} h_k \frac{f_{\sigma}(\bar{\rho}_k)}{\hat{\sigma}_{eq}^{(k)}(\bar{\rho})} \mathbf{H}_k^T \mathbf{a}_k, \quad (\text{B14})$$

where

$$\mathbf{a}_k = \mathbf{B}_k^T \mathbf{C}^0 \mathbf{M} \mathbf{C}^0 \mathbf{B}_k \mathbf{u}_k(\bar{\rho}). \quad (\text{B15})$$

After obtaining the derivatives with respect to the physical relative densities, Equation (B9), the chain rule is applied, as shown in references^{36,55}, in order to achieve the gradient of the AL function with respect to the design variables. The particularization to the pure EP approach is simply performed by considering $\mu_n = 0$ in Equation (B13).

B.2 P -mean

The adjoint method is used to compute the derivative of the P -mean constraint with respect to a physical relative density $\bar{\rho}_n$. The P -mean constraint in Equation (7) is rewritten as

$$g_{PM} = \left[\frac{1}{N_k} \sum_{k=1}^{N_k} \left(\frac{\sigma_{eq}^{(k)}(\bar{\rho})}{f_{\alpha}(\sigma_y)} \right)^P \right]^{\frac{1}{P}} - 1 + \zeta^T (\mathbf{K}(\bar{\rho}) \mathbf{U}(\bar{\rho}) - \mathbf{F}), \quad (\text{B16})$$

where ζ is the adjoint vector, which is arbitrary. The derivative of Equation (B16) is developed by employing the step-by-step procedure presented in da Silva et al.⁵, with straightforward modifications; thus, just the final derivative is shown, as follows

$$\frac{\partial g_{PM}}{\partial \bar{\rho}_n} = s_n \frac{\partial f_{\sigma}(\bar{\rho}_n)}{\partial \bar{\rho}_n} \hat{\sigma}_{eq}^{(n)}(\bar{\rho}) + \zeta_n^T \frac{\partial \mathbf{k}_n(\bar{\rho}_n)}{\partial \bar{\rho}_n} \mathbf{u}_n(\bar{\rho}), \quad (\text{B17})$$

where

$$s_n = \left(\frac{\sigma_{eq}^{(n)}(\bar{\rho})}{f_{\alpha}(\sigma_y)} \right)^{P-1} \frac{1}{N_k f_{\alpha}(\sigma_y)} \left[\frac{1}{N_k} \sum_{k=1}^{N_k} \left(\frac{\sigma_{eq}^{(k)}(\bar{\rho})}{f_{\alpha}(\sigma_y)} \right)^P \right]^{\frac{1}{P}-1}. \quad (\text{B18})$$

The local adjoint vector is computed as $\zeta_n = \mathbf{H}_n \zeta$. The global adjoint vector is obtained by solving the following system of linear equations

$$\mathbf{K}(\bar{\rho}) \zeta = - \sum_{k=1}^{N_k} s_k \frac{f_{\sigma}(\bar{\rho}_k)}{\hat{\sigma}_{eq}^{(k)}(\bar{\rho})} \mathbf{H}_k^T \mathbf{a}_k. \quad (\text{B19})$$

The derivatives of the volume fraction, Equation (B10), and P -mean constraint, Equation (B17), are corrected using the chain rule^{36,55}, in order to obtain both gradients with respect to the design variables.

C COMPLEMENTARY NUMERICAL RESULTS

For the sake of completeness, the L-shaped design problem is addressed using four alternative aggregation functions other than P -mean, as follows: P -norm, lower bound KS, upper bound KS, and Heaviside aggregation. The original optimization problem with global stress constraint is the same, Equation (6); the smoothed version, as shown in Equation (7) for P -mean, however, differs in writing of the stress constraint. The respective smoothed global stress constraints are given as follows.

- P -norm⁶:

$$g_{PN} = \sigma_{PN} - 1 \leq 0, \text{ where } \sigma_{PN} = \left[\sum_{k=1}^{N_k} \left(\frac{\sigma_{eq}^{(k)}(\bar{\rho})}{f_{\alpha}(\sigma_y)} \right)^P \right]^{\frac{1}{P}}. \quad (\text{C20})$$

- Lower bound KS⁷:

$$g_{LKS} = \sigma_{LKS} - 1 \leq 0, \text{ where } \sigma_{LKS} = \frac{1}{P} \ln \left(\frac{1}{N_k} \sum_{k=1}^{N_k} \exp \left(P \frac{\sigma_{eq}^{(k)}(\bar{\rho})}{f_{\alpha}(\sigma_y)} \right) \right). \quad (\text{C21})$$

- Upper bound KS⁷:

$$g_{UKS} = \sigma_{UKS} - 1 \leq 0, \text{ where } \sigma_{UKS} = \frac{1}{P} \ln \left(\sum_{k=1}^{N_k} \exp \left(P \frac{\sigma_{eq}^{(k)}(\bar{\rho})}{f_{\alpha}(\sigma_y)} \right) \right). \quad (C22)$$

- Heaviside aggregation⁴⁵:

$$g_{HPI} = \frac{\sum_{e=1}^{N_e} V_e H_{\theta} \left(\frac{\sigma_{eq}^{(e)}(\bar{\rho}) - f_{\alpha}(\sigma_y)}{f_{\alpha}(\sigma_y)} \right) \left(\frac{\sigma_{eq}^{(e)}(\bar{\rho})}{f_{\alpha}(\sigma_y)} \right)^{\eta_h}}{\sum_{e=1}^{N_e} V_e} - \epsilon \leq 0, \quad (C23)$$

where

$$H_{\theta} \left(\frac{\sigma_{eq}^{(e)}(\bar{\rho}) - f_{\alpha}(\sigma_y)}{f_{\alpha}(\sigma_y)} \right) = \frac{1}{2} + \frac{1}{\pi} \arctan \left(\frac{\sigma_{eq}^{(e)}(\bar{\rho}) - f_{\alpha}(\sigma_y)}{\theta f_{\alpha}(\sigma_y)} \right). \quad (C24)$$

In Equations (C20), (C21) and (C22), related to the P -norm, lower bound KS and upper bound KS, respectively, P is the penalty factor that controls the accuracy of the approximation. These aggregation functions work as the P -mean approach: for $P \rightarrow \infty$, the maximum value is recovered. The solution strategies are defined based on the Global 4 approach and $P = 60$, which turned out to be the most efficient global strategy. The yield stress function is computed using $\alpha = 1$, i.e., $f_{\alpha}(\sigma_y) = \sigma_y$. The solution strategies are given as follows.

Global 5: Fixed $P + c_{PN}$ normalization (1 it). Same as Global 4, with P -norm instead of P -mean to smooth the maximum operator; c_{PN} is updated using Equation (14), with σ_{PN} instead of σ_{PM} ; $c_{PN}^{(0)} = 1$.

Global 6: Fixed $P + c_{LKS}$ normalization (1 it). Same as Global 4, with lower bound KS instead of P -mean to smooth the maximum operator; c_{LKS} is updated using Equation (14), with σ_{LKS} instead of σ_{PM} ; $c_{LKS}^{(0)} = 1$.

Global 7: Fixed $P + c_{UKS}$ normalization (1 it). Same as Global 4, with upper bound KS instead of P -mean to smooth the maximum operator; c_{UKS} is updated using Equation (14), with σ_{UKS} instead of σ_{PM} ; $c_{UKS}^{(0)} = 1$.

In Equation (C23), θ is the Heaviside parameter, η_h is a penalty factor, and ϵ is the integral bound⁴⁵. The motivation behind the use of each of these parameters is presented by Wang and Qian⁴⁵, and it is out of the scope of this paper, so it is not repeated herein. Following Wang and Qian⁴⁵, we choose $\theta = 0.005$, $\eta_h = 2$, and ϵ is set to 0.005 at the first 25 iterations and to 0.0025 in the following 25 iterations; then, it is updated every 10 iterations by using the following relation⁴⁵

$$\epsilon^{(b)} = \min \left\{ \frac{\epsilon^{(b-1)}}{\tilde{\sigma}_{max}}, \epsilon^{(b-1)} \right\}, \quad (C25)$$

where $\tilde{\sigma}_{max}$ is the average of the maximum normalized von Mises stresses in the previous five iterations. Based on the above, we define the following global strategy.

Global 8: Heaviside aggregation. The problem is addressed with the Heaviside aggregation approach following the hints by Wang and Qian⁴⁵, except for β , which is updated every 20 iterations using Equation (12). The yield stress function is computed using $\alpha = 1$, i.e., $f_{\alpha}(\sigma_y) = \sigma_y$.

The L-shaped problem is addressed considering the same input data, mesh resolution, and stopping criteria as employed in subsection 6.1, using $nit_{min} = 500$ and $nit_{max} = 2000$. Figure C1 shows the optimized topologies and respective von Mises equivalent stress fields.

The results shown in Figure C1 are comparable to the ones presented in second row of Figures 7 and 8, related to the four local solution strategies, and in second row of Figures 9 and 10, related to the four P -mean global solution strategies. Figure C2 shows the volume fractions of the optimized topologies obtained with all local and global solution strategies with respect to the total number of iterations. The result that violates the stress constraint the most is highlighted, related to the Global 2 strategy; the other stress constraint violations ($< 0.2\%$), also related to the global strategies, are omitted.

Analyzing Figure C2, one can verify that none of the approaches presented in this appendix (i.e., Global strategies 5, 6, 7 and 8) is able to outperform the local solution strategies in neither performance nor efficiency. The only global approaches able to match some of the local strategies are Global strategies 1 and 4; the former is better than Local 4 strategy regarding efficiency, but much worse regarding performance; the latter is better than Local strategies 1, 3 and 4 regarding performance, but much worse regarding efficiency. Thus, based on the above results and observations, one can verify that the concluding remarks of this paper also apply for the other aggregation functions and algorithmic settings investigated in this appendix.

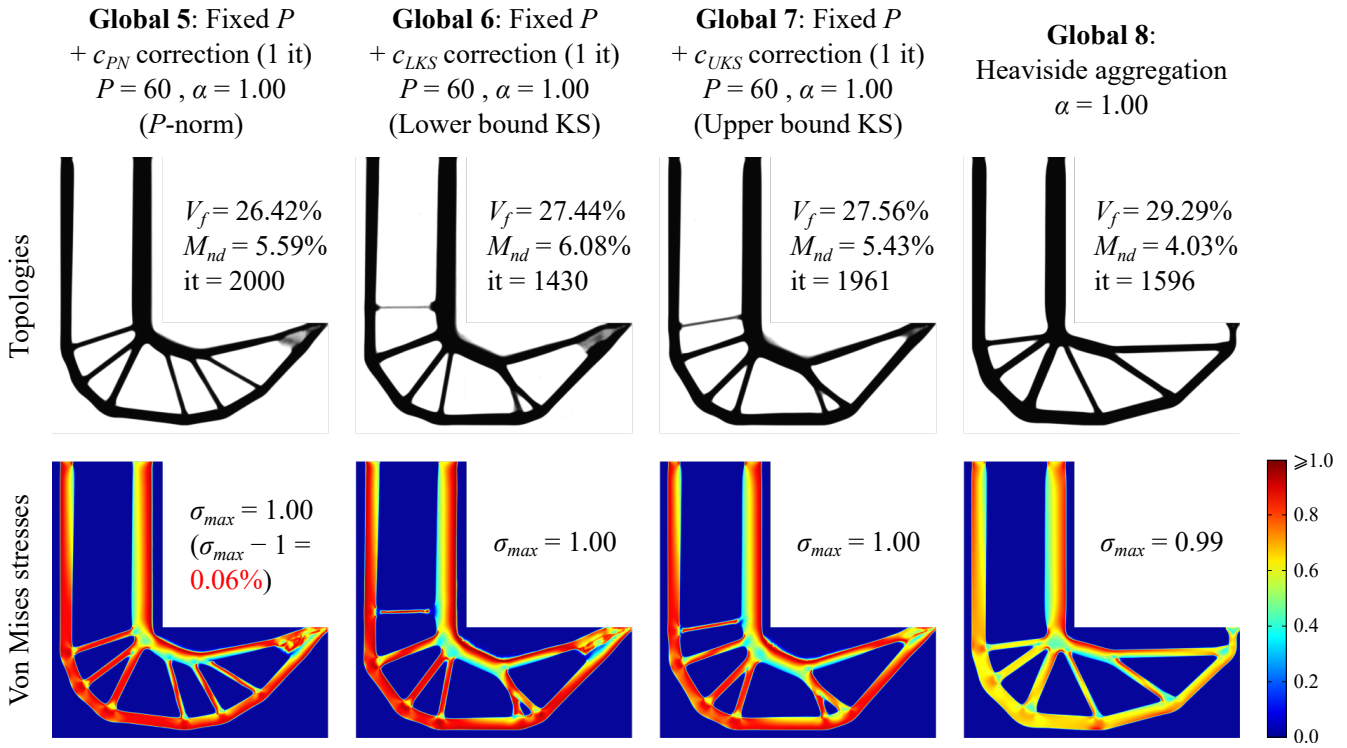


FIGURE C1 Optimized topologies and respective von Mises stress fields, Global strategies 5, 6, 7 and 8.

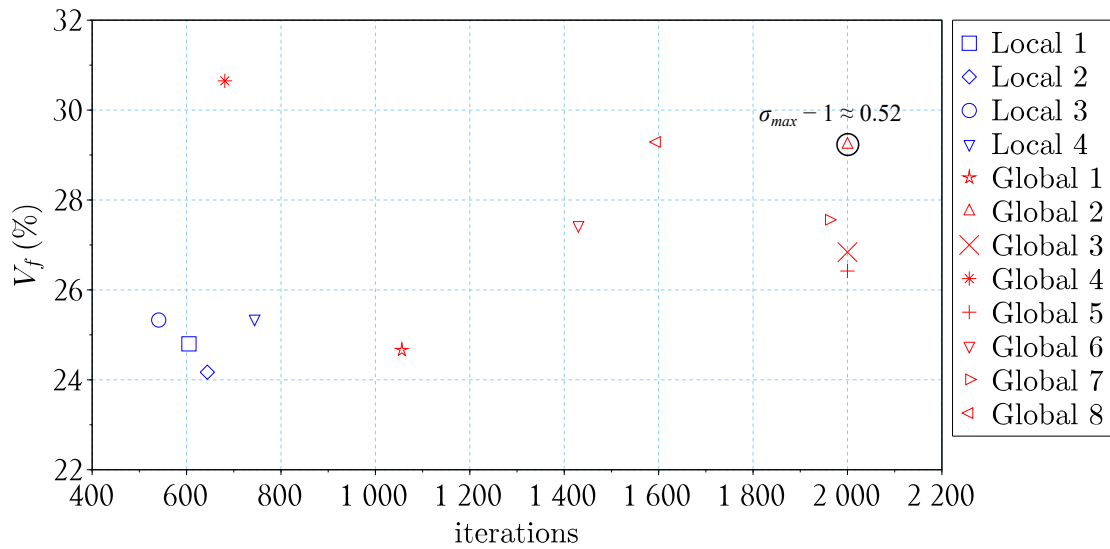


FIGURE C2 Volume fractions of L-shaped optimized topologies obtained with all local and global solution strategies, using $nit_{min} = 500$ and 800×800 mesh resolution. The results are placed on the number of iterations that each strategy took to reach the stopping criteria.

D ITERATION GRAPHS

Figures D3 and D4 show the iteration histories of the volume fraction, V_f , and maximum von Mises equivalent stress normalized by the yield stress value, σ_{max} , for the four local strategies results shown in Table 1. Figures D5 and D6 show the volume and stress iteration histories for the four global strategies results shown in Table 2.

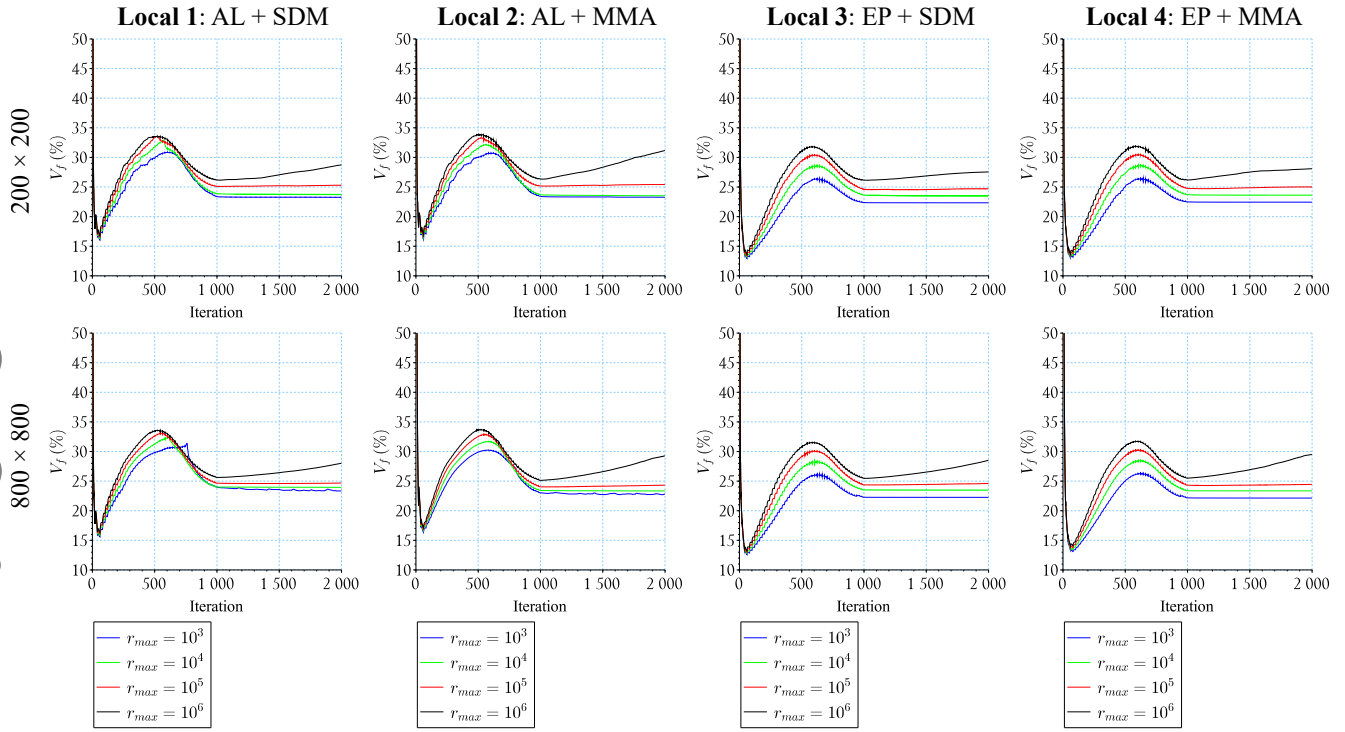


FIGURE D3 Volume fraction iteration histories of the local strategies for different r_{max} and two mesh resolutions.

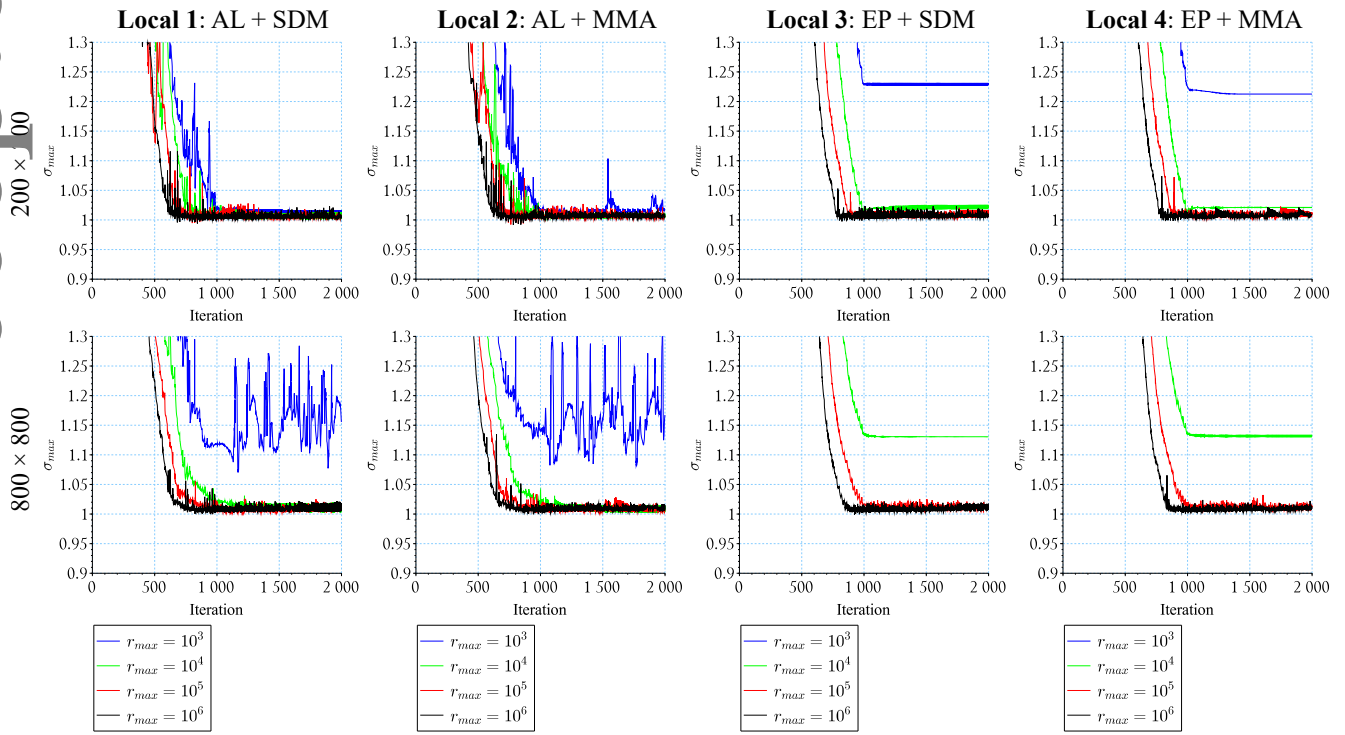


FIGURE D4 Maximum von Mises stress iteration histories of the local strategies for different r_{max} and two mesh resolutions.

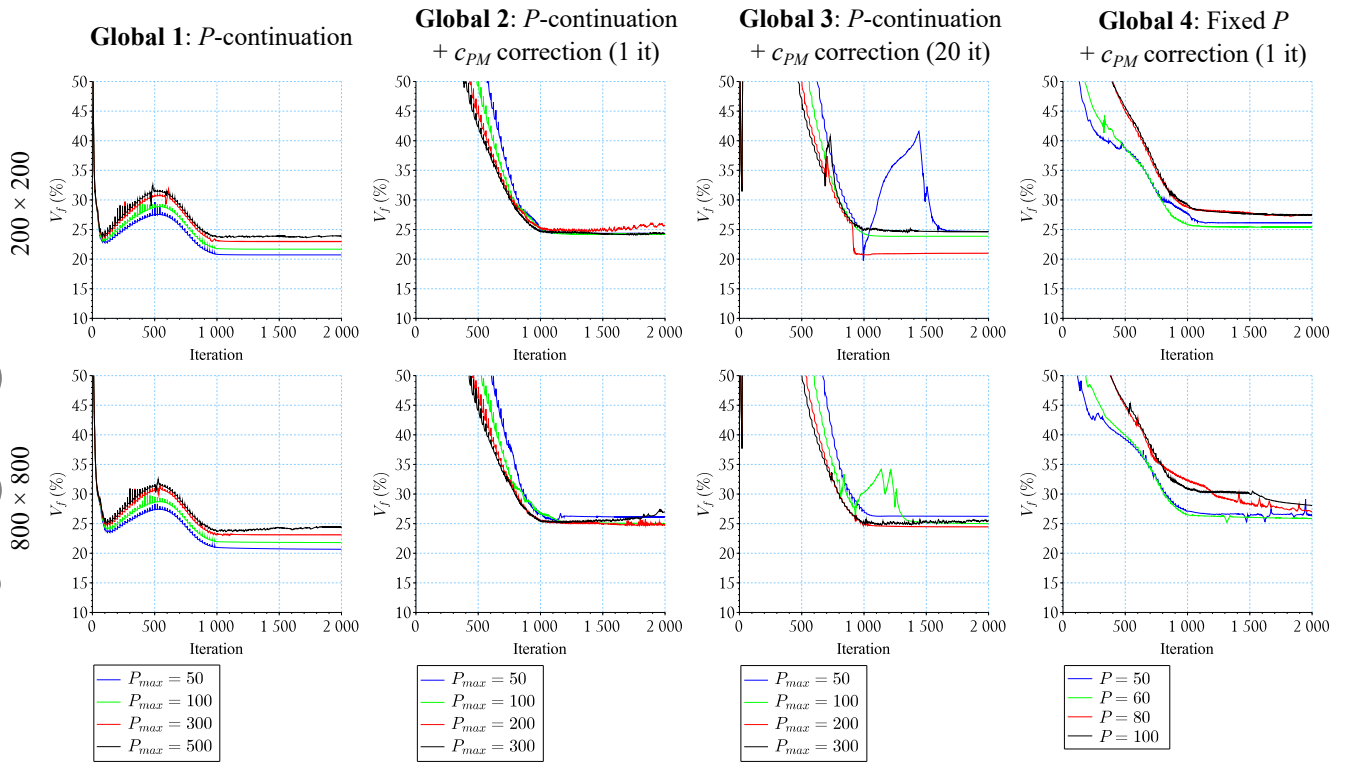


FIGURE D5 Volume fraction iteration histories of the global strategies for different P_{max} and two mesh resolutions.

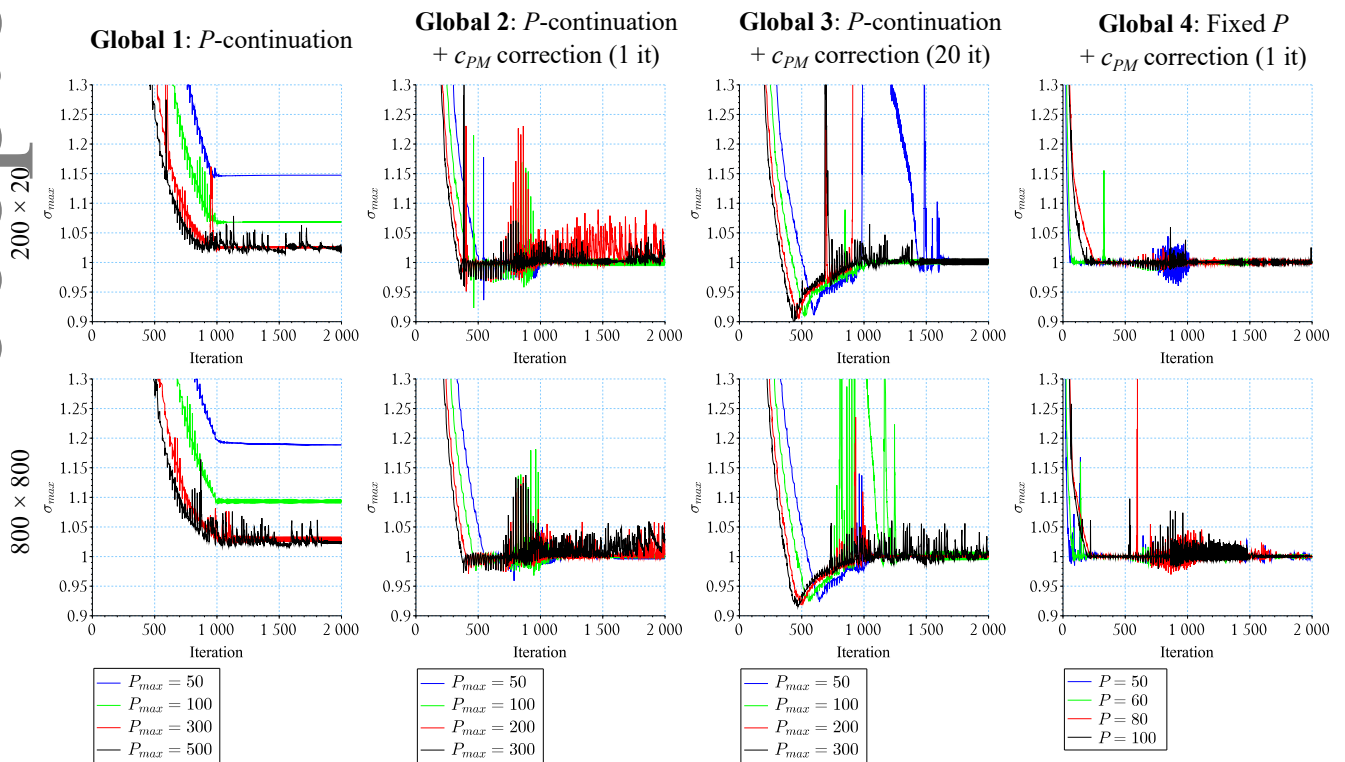


FIGURE D6 Maximum von Mises stress iteration histories of the global strategies for different P_{max} and two mesh resolutions.